

Generation of 95-qubit genuine entanglement and verification of symmetry-protected topological phases

Tao Jiang,^{1,2,3,*} Jianbin Cai,^{1,2,3,*} Junxiang Huang,^{4,5,*} Naibin Zhou,^{1,2,3,*} Yukun Zhang,^{4,5} Jiahao Bei,² Guoqing Cai,² Sirui Cao,^{1,2,3} Fusheng Chen,^{1,2,3} Jiang Chen,² Kefu Chen,^{1,2,3} Xiawei Chen,² Xiqing Chen,² Zhe Chen,⁶ Zhiyuan Chen,^{1,2,3} Zihua Chen,^{1,2,3} Wenhao Chu,⁶ Hui Deng,^{1,2,3} Zhibin Deng,² Pei Ding,² Xun Ding,³ Zhuzhengqi Ding,² Shuai Dong,² Bo Fan,² Daojin Fan,^{1,2,3} Yuanhao Fu,^{1,2,3} Dongxin Gao,^{1,2,3} Lei Ge,² Jiacheng Gui,³ Cheng Guo,^{1,2,3} Shaojun Guo,^{1,2,3} Xiaoyang Guo,² Lianchen Han,^{1,2,3} Tan He,^{1,2,3} Linyin Hong,⁶ Yisen Hu,^{1,2,3} He-Liang Huang,⁷ Yong-Heng Huo,^{1,2,3} Zuokai Jiang,² Honghong Jin,² Yunxiang Leng,² Dayu Li,^{1,2,3} Dongdong Li,⁶ Fangyu Li,² Jiaqi Li,² Jinjin Li,^{3,8} Junyan Li,² Junyun Li,^{1,2,3} Na Li,^{1,2,3} Shaowei Li,^{1,2,3} Wei Li,² Yuhuai Li,^{1,2,3} Yuan Li,^{1,2,3} Futian Liang,^{1,2,3} Xuelian Liang,⁹ Nanxing Liao,² Jin Lin,^{1,2,3} Weiping Lin,^{1,2,3} Dailin Liu,³ Hongxiu Liu,² Maliang Liu,¹⁰ Xinyu Liu,³ Xuemeng Liu,⁶ Yancheng Liu,^{1,2,3} Haoxin Lou,² Yuwei Ma,^{1,2,3} Lingxin Meng,² Hao Mou,² Kailiang Nan,³ Binghan Nie,² Meijuan Nie,² Jie Ning,⁹ Le Niu,² Wenyi Peng,³ Haoran Qian,^{1,2,3} Hao Rong,^{1,2,3} Tao Rong,^{1,2,3} Huiyan Shen,⁶ Qiong Shen,² Hong Su,^{1,2,3} Feifan Su,^{1,2,3} Chenyin Sun,^{1,2,3} Liangchao Sun,⁶ Tianzuo Sun,^{1,2,3} Yingxiu Sun,⁶ Yimeng Tan,² Jun Tan,³ Longyue Tang,² Wenbing Tu,⁶ Jiafei Wang,⁶ Biao Wang,⁶ Chang Wang,⁶ Chen Wang,^{1,2,3} Chu Wang,^{1,2,3} Jian Wang,³ Liangyuan Wang,² Rui Wang,^{1,2,3} Shengtao Wang,³ Xiaomin Wang,⁹ Xinzhe Wang,³ Xunxun Wang,⁹ Yeru Wang,⁹ Zuolin Wei,^{1,2,3} Jiazhou Wei,⁶ Dachao Wu,^{1,2,3} Gang Wu,^{1,2,3} Jin Wu,³ Yulin Wu,^{1,2,3} Shiyong Xie,³ Lianjie Xin,⁹ Yu Xu,^{1,2,3} Chun Xue,⁶ Kai Yan,^{1,2,3} Weifeng Yang,⁶ Xinpeng Yang,^{1,2,3} Yang Yang,² Yangsen Ye,^{1,2,3} Zhenping Ye,^{1,2,3} Chong Ying,^{1,2,3} Jiale Yu,^{1,2,3} Qinjing Yu,^{1,2,3} Wenhui Yu,² Xiangdong Zeng,¹ Chen Zha,^{1,2,3} Shaoyu Zhan,^{1,2,3} Feifei Zhang,² Haibin Zhang,³ Kaili Zhang,² Wen Zhang,² Yiming Zhang,^{1,2,3} Yongzhuo Zhang,³ Lixiang Zhang,⁶ Guming Zhao,^{1,2,3} Peng Zhao,^{1,2,3} Xintao Zhao,² Youwei Zhao,^{1,2,3} Zhong Zhao,⁶ Luyuan Zheng,² Fei Zhou,⁹ Liang Zhou,⁶ Na Zhou,² Shifeng Zhou,³ Shuang Zhou,³ Zhengxiao Zhou,³ Chengjun Zhu,³ Qingling Zhu,^{1,2,3} Guihong Zou,³ Haonan Zou,² Qiang Zhang,^{1,2,3,9} Chao-Yang Lu,^{1,2,3} Cheng-Zhi Peng,^{1,2,3} Xiao Yuan,^{4,5} Ming Gong,^{1,2,3} Xiaobo Zhu,^{1,2,3,9} and Jian-Wei Pan^{1,2,3}

¹*Hefei National Research Center for Physical Sciences at the Microscale and School of Physical Sciences, University of Science and Technology of China, Hefei 230026, China*

²*Shanghai Research Center for Quantum Science and CAS Center for Excellence in Quantum Information and Quantum Physics, University of Science and Technology of China, Shanghai 201315, China*

³*Hefei National Laboratory, University of Science and Technology of China, Hefei 230088, China*

⁴*Center on Frontiers of Computing Studies, Peking University, Beijing 100871, China*

⁵*School of Computer Science, Peking University, Beijing 100871, China*

⁶*QuantumCTek Co., Ltd., Hefei 230088, China*

⁷*Henan Key Laboratory of Quantum Information and Cryptography, Zhengzhou, Henan 450000, China*

⁸*National Institute of Metrology, Beijing 102200, China*

⁹*Jinan Institute of Quantum Technology and Hefei National Laboratory Jinan Branch, Jinan 250101, China*

¹⁰*School of Microelectronics, Xidian University, Xi'an, China*

(Dated: May 6, 2025)

Abstract

Symmetry-protected topological (SPT) phases [1] are fundamental features of cluster states, serving as key resources for measurement-based quantum computation (MBQC) [2, 3]. Generating large-scale cluster states and verifying their SPT phases are essential steps toward practical MBQC, which however still presents significant experimental challenges. In this work, we address these challenges by utilizing advanced superconducting hardware with optimized gate operations, enhanced readout fidelity, and error mitigation techniques [4]. We successfully generate and verify 95-qubit one-dimensional and 72-qubit two-dimensional genuine entangled cluster states, achieving fidelities of 0.5603 ± 0.0084 and 0.5519 ± 0.0054 , respectively. Leveraging these high-fidelity cluster states, we investigate SPT phases through quantum teleportation across all 95 qubits and demonstrate input-state-dependent robustness against symmetry-breaking perturbations, highlighting the practicality and intrinsic robustness of MBQC enabled by the SPT order. Our results represent a significant advancement in large-scale entanglement generation and topological phase simulation, laying the foundation for scalable and practical MBQC using superconducting quantum systems.

I. INTRODUCTION

Entanglement is a crucial resource in quantum information processing [5, 6] and plays a foundational role in many-body physics [7] and quantum computing algorithms [8, 9]. The generation of large-scale entangled states has become a central focus in quantum computing experiments, serving as both a benchmark for quantum hardware capability and a crucial step toward achieving universal quantum computation [10–14]. In recent years, substantial efforts have been dedicated to generating multi-partite entangled states, such as the Greenberger–Horne–Zeilinger (GHZ) states [15–17] and cluster states [18–20]. We observe a phenomenon resembling quantum Moore’s law, where the number of entangled qubits doubles approximately every one or two years. However, this progress is not simply due to an increase in the number of qubits; it is also driven by significant advancements in quantum hardware, including more accurate quantum gates, improved readout precision, and longer decoherence times. Despite these advances, many implementations still face limitations imposed by design constraints and inherent noise, which restrict the size and scalability of the

* These authors contributed equally to this work.

entangled states [21, 22]. A key question, then, is whether we can continue to follow the trajectory of quantum Moore’s law with the current state of quantum technology.

Another critical question is how to utilize the generated entangled states in real experimental applications. While the GHZ state has been created and used to study phenomena such as the Nishimori transition [23] and discrete time crystals [24], the broader application of multipartite entanglement in real-world experiments and many-body physics is still in its early stages. On the other hand, cluster states are a key resource for measurement-based quantum computation (MBQC) [2, 3, 25, 26] and measurement-based variational quantum eigensolver [27]; yet, existing proof-of-principle experiments have been limited to very small-scale problems [28, 29], and their scalability to larger problems remains an open question. Therefore, another challenge is to explore how entanglement can be harnessed for large-scale quantum simulation and computation.

Here, we tackle these challenges using *Zuchongzhi* 3.1, a 105-qubit superconducting quantum processor with significantly improved energy relaxation time, readout fidelity, and two-qubit CZ gate fidelity, as shown in Fig. 1a. These enhancements result from systematic electric field configuration optimization [30], an improved readout design [31] incorporating traveling-wave parametric amplifiers (TWPA) [32], and dynamically optimized parallel CZ gate parameters. As a result, we achieve the preparation of genuine entangled cluster states with up to 95 qubits, nearly doubling the previous record. This advancement in large-scale entanglement generation establishes a robust platform for exploring complex many-body physics and measurement-based quantum computation, as illustrated in Fig. 1b. Since the symmetry-protected topological (SPT) nature [1, 33] of cluster states is a fundamental resource for MBQC, we explored the SPT phases of high-fidelity one-dimensional (1D) cluster states. We successfully demonstrated high-fidelity quantum teleportation across a 95-qubit 1D cluster state and investigated the robustness of the teleportation process under both symmetry-preserving and symmetry-breaking local perturbations. These findings provide valuable insights into the feasibility of MBQC using state-of-the-art superconducting quantum hardware.

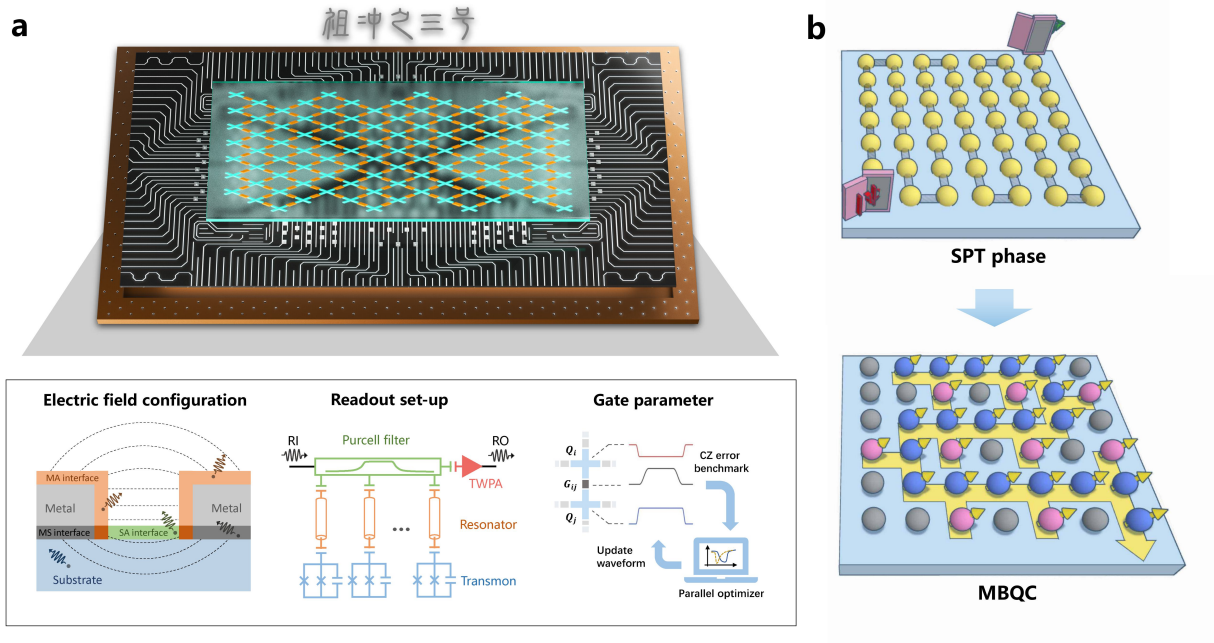


FIG. 1. Chip architecture, key technologies, and applications of the *Zuchongzhi 3.1* processor. (a) Schematic diagram of the *Zuchongzhi 3.1* processor architecture and key technological innovations. The processor employs a flip-chip integration design, with the top chip containing 105 transmon qubits and 182 tunable couplers, while the bottom chip integrates readout resonators alongside control lines. To enable large-scale cluster state generation, we optimized the electric field configuration to enhance qubit coherence times, improved the readout design and incorporated traveling-wave parametric amplifiers to achieve higher readout fidelity, and dynamically optimized parallel CZ gate parameters to enhance two-qubit gate fidelity. (b) Potential applications of the generated high-fidelity cluster states. One-dimensional cluster states enable the investigation of symmetry-protected topological phases via quantum teleportation experiments. Two-dimensional cluster states provide a platform for measurement-based quantum computation.

II. CLUSTER STATE PREPARATION AND WITNESS

We first introduce the implementation of 1D and 2D cluster states. Consider an n -vertex graph $G(V, E)$ with vertices V and edges E , a stabilizer operator g_i for each vertex i is $S_i := X_i \otimes_{j \in \mathcal{N}(i)} Z_j$, where $\mathcal{N}(i)$ denotes the set of neighbors of vertex i , i.e., $\mathcal{N}(i) = \{x \mid x \in V, (x, i) \in E\}$, and X_i, Y_i, Z_i are the Pauli operators acting on the i -th qubit. The cluster state $|\text{CL}\rangle$ is the common eigenstate of all stabilizers: $S_i|\text{CL}\rangle = |\text{CL}\rangle, \quad \forall i = 1, \dots, n.$

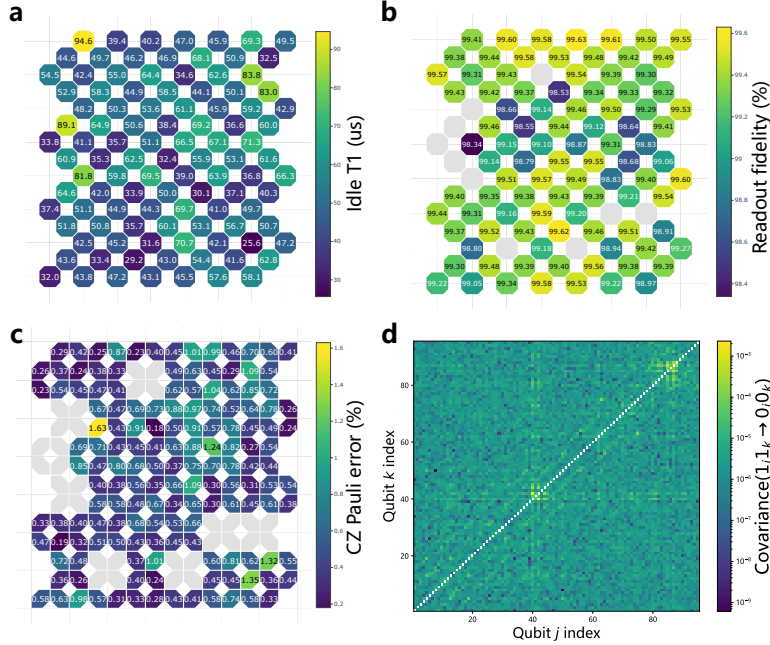


FIG. 2. Key performances of the processor. (a) Energy relaxation time T_1 : the median T_1 of all 105 qubits at idle frequencies is $49.7 \mu\text{s}$. (b) Readout fidelity: the median readout fidelity of 95 measured qubits using random state preparation schemes [18] is 99.35%. (c) Two-qubit gate fidelity: the median fidelity of 150 calibrated CZ gates is 99.50%. (d) Covariance matrix of the readout errors $1_j 1_k$ to $0_j 0_k$ for the 95 measured qubits in the 1D topology. Off-diagonal elements indicate correlated errors, with color intensity on a logarithmic scale reflecting the magnitude of the covariance.

Equivalently, the cluster state $|\text{CL}\rangle$ has an explicit form $|\text{CL}\rangle = \prod_{(i,j) \in E} \text{CZ}_{(i,j)}|+\rangle^{\otimes n}$, where $\text{CZ}_{(i,j)}$ represents the controlled- Z gate acting on qubits i and j , and $|+\rangle = (|0\rangle + |1\rangle)/\sqrt{2}$. This form illustrates how cluster states can be constructively prepared from the computational basis states using a series of CZ gates. For the experimentally prepared cluster state $\hat{\rho}_{\text{CL}}$, we can measure the fidelity $F = \langle \text{CL} | \hat{\rho}_{\text{CL}} | \text{CL} \rangle$ and certify genuine multipartite entanglement whenever $F > 50\%$ [34]. Measuring the fidelity requires implementing the projector $|\text{CL}\rangle\langle \text{CL}| = \prod_{i \in V} (\mathbb{I} + S_i)/2$, which can be efficiently obtained by randomly measuring Pauli operators $P^{(m)} = \prod_{i=1}^n P_i^{(m)}$ with each $P_i^{(m)}$ randomly drawn from $\{\mathbb{I}, S_i\}$ [35].

To achieve high-fidelity and large-scale cluster states, we have introduced several key hardware enhancements that significantly improve the performance of the quantum processor. Drawing on multiple studies examining the relationship between qubit layout, surface

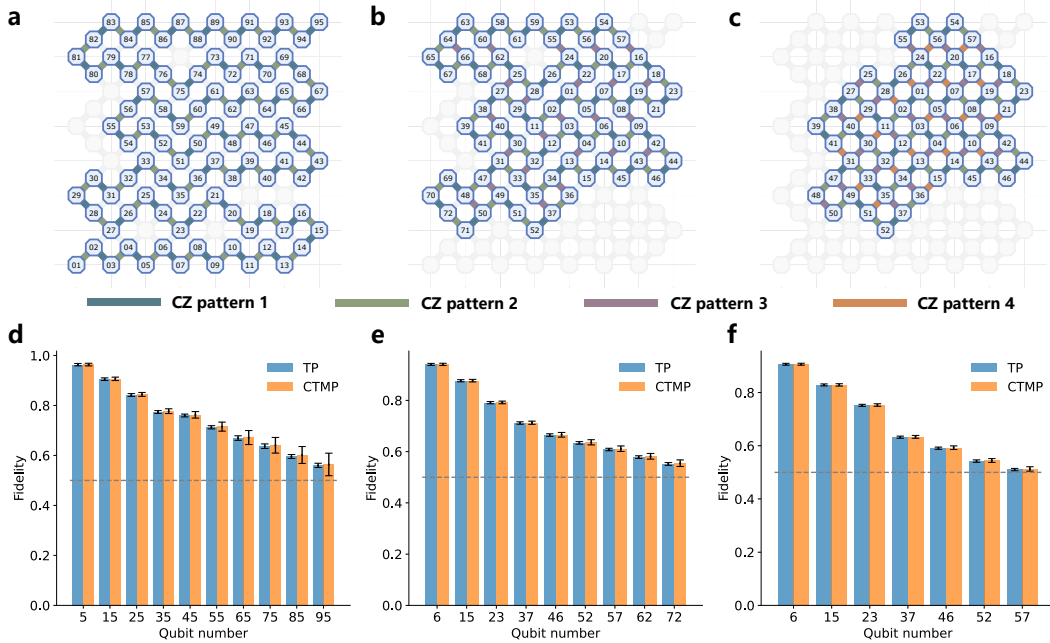


FIG. 3. Layout and fidelity of 1D and 2D cluster states. (a) Layout of a 1D cluster state geometry with 95 qubits and two CZ patterns. (b) Layout of a 2D cluster state geometry with 72 qubits and three CZ patterns. (c) Layout of a 2D cluster state geometry with 57 qubits and four CZ patterns. (d, e, f) Cluster state fidelity as a function of qubit number with different readout error mitigation strategy, including (d) 1D, (e) 2D sparse, and (f) 2D full cluster state. Since the correlated noise between qubit pairs is relatively weak, we can use the tensor product method for readout error mitigation, whereas we can also consider the most correlated two-qubit correlations to build the correction matrix within the framework of continuous-time Markov processes. The error bars in (d), (e) and (f) represent the confidence interval of 99.7%. The grey dashed line corresponds to the fidelity of 50%. The total measurement time was 26 hours.

participation, and dielectric loss, we optimized the electric field configuration within the tunable-coupler architecture. Additionally, we employed tantalum [36] to further enhance qubit lifetime. These improvements led to a 1.6 times increase in the median energy relaxation time, extending it from $30.8 \mu\text{s}$ [37] to $49.7 \mu\text{s}$, as shown in Fig. 2a. We also updated the design of the Purcell filter to optimize the coupling g and photon-loss rate κ of the readout resonators and developed a traveling wave parametric amplifier to further enhance the signal-to-noise ratio of the readout, improving the readout fidelity from 95.09% [18] to 99.35%, as shown in Fig. 2b. Additionally, we implemented a range of optimization strate-

gies, including frequency arrangement and parallel optimization of gate parameters, which improved the median two-qubit CZ gate fidelity from 99.05% [18] to 99.50%, with all 150 calibrated gates shown in Fig. 2c.

The quantum circuit for cluster state preparation begins with a layer of \sqrt{Y} gates to initialize all qubits to the $|+\rangle$ state, followed by layers of parallel CZ gates applied sequentially to entangle the qubits. To address readout errors in the circuit, we utilized multiple error models to characterize and mitigate noise effects [4]. Specifically, we measured the outcomes of 21,500 randomized initial states on the system involving 95 qubits, with each state subjected to 3,000 single-shot measurements, providing a comprehensive characterization of the system readout errors. The dataset enabled us to estimate two-qubit correlated noise and calculate correlation coefficients for selected qubit pairs, identifying key sources of error correlations. As exemplified in Fig. 2d, for the correlated readout error $1_j 1_k$ to $0_j 0_k$, which is defined as the covariance of events that 1_j and 1_k flips, the median correlation is 2.09×10^{-6} , with a maximum of 2.30×10^{-3} , suggesting that most correlated noise between qubit pairs is relatively weak. This observation supports the approach of treating qubit noise as approximately independent, which allows for the cancellation of both independent and correlated readout errors within the tensor product (TP) and continuous-time Markov process (CTMP) schemes, respectively.

For the 1D cluster state, we used the topology depicted in Fig. 3a. To evaluate the fidelity of the 95-qubit 1D cluster state, we uniformly sampled $M = 3490$ stabilizers and performed $K = 3000$ single-shot measurements per stabilizer. Under independent TP readout error mitigation, the fidelity of the 95-qubit 1D cluster state was certified as 0.5603 ± 0.0084 with a confidence level exceeding 99.7%. After analyzing the fidelity results for the stabilizers (see Supplementary Materials), we observed that the fidelity distribution follows a composite Gaussian-type form with a standard deviation of 0.064. This results in an overall average uncertainty of 0.0032 within the 99.7% confidence interval. These findings confirm the stability of our system, as the uncertainty – accounting for both systematic and statistical errors – remains well below the theoretically estimated error.

To further evaluate the effect of readout correlations, we utilize the CTMP scheme [4] to address correlated errors between qubits. Unlike traditional models that assume independent noise sources, the CTMP framework incorporates noise generators, G_i , that correspond to specific error types, including single-qubit bit-flip errors and two-qubit correlated bit-flip

errors. The evolution of the noise is governed by the matrix exponential $\Lambda = \exp(G)$, where $G = \sum_i r_i G_i$ is the sum of these generators, weighted by error rate coefficients r_i . For noise inversion, we employ a sampling-based method that avoids the computational complexity of direct matrix inversion. Instead, we sample from a Poisson distribution to compute the weighted sum, simulating the inverse effects of noise interactions. This approach enables efficient noise simulation, prioritizing significant correlated errors, and scales well for larger quantum systems. After applying error mitigation, we obtain a fidelity of 0.5639 ± 0.0453 for the 95-qubit case, with a confidence level exceeding 99.7%. A more detailed analysis of correlated readout errors and the associated error mitigation overhead is provided in the Supplementary Materials. Fig. 3d compares the fidelities obtained from both TP and CTMP methods, from 5 to 95 qubits, illustrating the negligible effect of readout correlations in our system.

For 2D cluster states, we implemented two distinct topologies: the three-pattern (“sparse”) topology and the four-pattern (“full”) topology, as shown in Fig. 3b and c. The key difference between these configurations is that the three-pattern topology can be derived from the four-pattern topology by removing the fourth layer of CZ gates, which allows for a larger 2D entanglement system while maintaining the same fidelity. For the 72-qubit 2D three-pattern cluster state, we uniformly sampled $M = 2393$ stabilizers, with each stabilizer undergoing $K = 2000$ single-shot measurements. For the 57-qubit 2D four-pattern cluster state, we sampled $M = 2002$ stabilizers, with the same number of single-shot measurements per stabilizer. We estimated the fidelities and associated errors for both topologies across a range of system sizes, from 6 qubits up to the maximum sizes of 72 qubits (three-pattern) and 57 qubits (four-pattern), as shown in Fig. 3e and f. The total measurement times were 16 hours and 6.5 hours, respectively. Notably, under independent error mitigation, the fidelities for the 72-qubit 2D three-pattern and 57-qubit 2D four-pattern cluster states are 0.5519 ± 0.0054 and 0.5104 ± 0.0045 , respectively, with a confidence level exceeding 99.7%. As a contrast, under correlated readout error mitigation, the fidelities for the 72-qubit and 57-qubit cluster states are 0.5549 ± 0.0127 and 0.5128 ± 0.0082 , respectively. The comparison of the fidelities under both error mitigation schemes shows the negligible effect of readout correlation on the fidelity results for these systems.

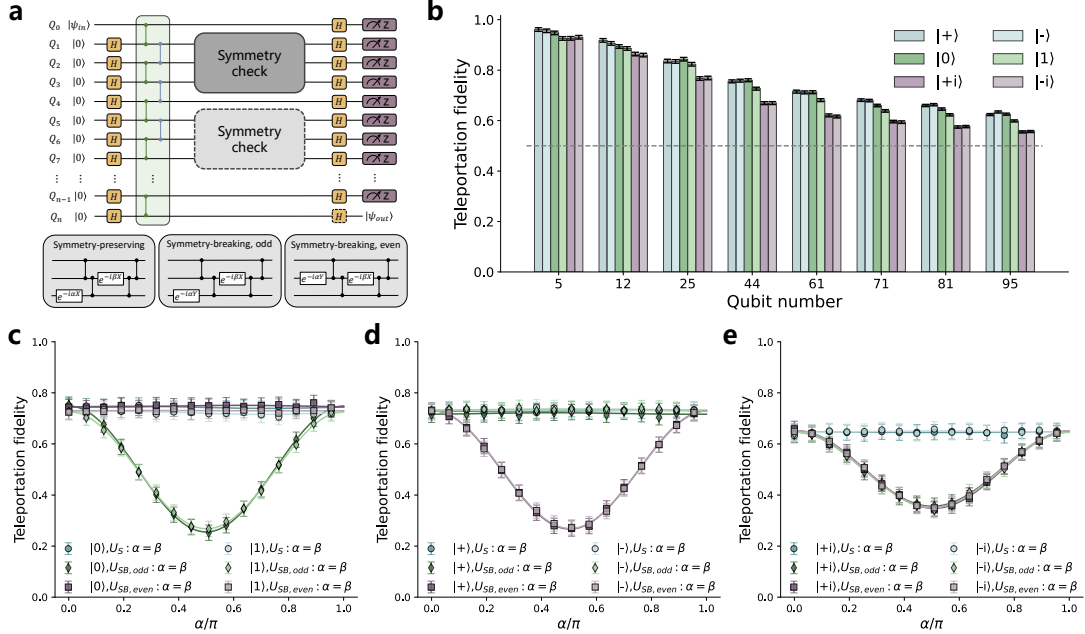


FIG. 4. Experimental simulation of SPT phases in quantum teleportation. (a) Quantum teleportation circuit for symmetry-protected topological phase experiments, where teleportation is realized through measurement after one-dimensional entanglement. The experiments investigate fidelity oscillations in quantum teleportation under three symmetry perturbations. (b) Teleportation fidelity as a function of total qubit number for various input states ($|+\rangle$, $|-\rangle$, $|0\rangle$, $|1\rangle$, $|+i\rangle$, $| -i\rangle$). The fidelity $F = |\langle \psi_{\text{in}} | \tilde{\psi}_{\text{out}} \rangle|^2$, where $|\tilde{\psi}_{\text{out}}\rangle = X^{\sum_{i \in \text{odd}} m_i} Z^{\sum_{i \in \text{even}} m_i + m_0} |\psi_{\text{out}}\rangle$, with Z and X being the Pauli operators, and m_i denotes the measurement outcomes (0 or 1) for the qubits indexed starting from 1. (c) (d) (e) Teleportation fidelity as a function of the phase parameter α for input states $|0\rangle$ and $|1\rangle$, $|+\rangle$ and $|-\rangle$, $|+i\rangle$ and $| -i\rangle$, respectively. Using a cluster state with $N = 24$, we explored the effects of different perturbations, including symmetry-preserving (circle), odd-parity symmetry-breaking (diamond), and even-parity symmetry-breaking (square).

III. SIMULATION OF SYMMETRY-PROTECTED TOPOLOGICAL PHASES

The intrinsic SPT properties of cluster states are essential for MBQC, making the verification of SPT phases in large-scale cluster states a critical step for their utilization in MBQC [38, 39]. Verifying the preservation of the $\mathbb{Z}_2 \times \mathbb{Z}_2$ symmetry is key to ensuring that the cluster state can function as a resource for MBQC, as the computational power of SPT phases arises from the symmetries they retain [40]. With the availability of high-fidelity

cluster states, we are now well-positioned to explore and study the SPT phase further [1, 33].

A 1D cluster state satisfies the $\mathbb{Z}_2 \times \mathbb{Z}_2$ symmetry, which is characterized by the odd-parity operator $P_{\text{odd}} = \prod_{i \in \text{odd}} S_i$ and the even-parity operator $P_{\text{even}} = \prod_{i \in \text{even}} S_i$ and serves as the key resource for MBQC. The SPT phase of the 1D cluster states can be certified by quantum teleportation [38], a special case of MBQC. Specifically, we teleport an input state $|\psi_{\text{in}}\rangle$ using a 1D cluster state by entangling them and measuring the intermediate qubits in the Pauli X-basis. The input state is then transferred to the output qubit, up to a unitary correction, as shown in Fig. 4a. The symmetry-protected nature of 1D cluster states implies that quantum teleportation remains robust as long as the underlying symmetry is preserved. This robustness can be leveraged to detect SPT orders and hence benchmark the feasibility of MBQC.

In our experiment, we first conducted a series of teleportation tasks with different input states and 1D cluster states with up to 94 nodes, as shown in Fig. 4b. The teleportation fidelity consistently exceeded 50% for all cases, certifying the SPT phase of the 1D cluster states. Notably, the fidelities for the $|+\rangle$, $|-\rangle$, $|0\rangle$, and $|1\rangle$ states consistently outperformed those for the $|+i\rangle$ and $|-i\rangle$ states. This indicates that the teleportation circuits could be affected differently by the noises for different input states.

We further investigated the SPT phases by introducing three symmetry-checking unitaries: $U_S(\alpha, \beta) = e^{i\beta Z_1 X_2 Z_3} e^{i\alpha X_3}$, $U_{\text{SB,odd}}(\alpha, \beta) = e^{i\beta Z_1 X_2 Z_3} e^{i\alpha Y_3}$, and $U_{\text{SB,even}}(\alpha, \beta) = e^{i\beta Z_1 X_2 Z_3} e^{i\alpha Y_2}$, corresponding to symmetry-preserving, odd-parity symmetry-breaking, and even-parity symmetry-breaking perturbations, respectively. As shown in Fig. 4c, for the input states $|0\rangle$ and $|1\rangle$, the fidelity of the teleportation was examined as a function of the phase α , revealing the effects of these perturbations. Significant fidelity oscillations were observed under odd-parity symmetry-breaking perturbations, while the fidelity remained robust for the other unitaries. For the $|+\rangle$ and $|-\rangle$ input states, as shown in Fig. 4d, the fidelity was influenced only by even-parity symmetry-breaking perturbations $U_{\text{SB,even}}$. Interestingly, for the $|+i\rangle$ and $|-i\rangle$ states, fidelity oscillations were observed under both odd- and even-parity symmetry-breaking perturbations, as shown in Fig. 4e.

This intriguing phenomenon arises from the fact that the success of quantum teleportation for different input stabilizer states depends on the preservation of either odd-parity (e.g., $|0\rangle$ and $|1\rangle$), even-parity (e.g., $|\pm\rangle$), or both parity operators (e.g., $|\pm i\rangle$). Notably, the symmetry-breaking unitary U_{SB} may act differently depending on which \mathbb{Z}_2 symmetry the

input state pertains to. Specifically, U_{SB} can break one of the $\mathbb{Z}_2 \times \mathbb{Z}_2$ symmetries (either odd or even), while leaving the other symmetry intact, thereby leaving input states that respect the unaffected symmetry unchanged. The implications are that when noise breaks the $\mathbb{Z}_2 \times \mathbb{Z}_2$ symmetry, the $|0\rangle$, $|1\rangle$, $|+\rangle$, and $|-\rangle$ input states are affected by the breaking of either the odd or even symmetry, but not both. However, the $|+i\rangle$ and $|-i\rangle$ states exhibit greater sensitivity to symmetry breaking, as evidenced by the experimental results shown in Fig. 4b, which demonstrate lower fidelities compared to the other input states. A more detailed explanation is provided in the Supplementary Materials. These findings underscore the intricate dependence of the SPT phases on the choice of input states and the application of symmetry-breaking operations, providing valuable insights into the robustness and detection of SPT phases in quantum systems.

IV. CONCLUSION

In this work, we have made significant strides in generating and verifying genuine entangled cluster states on superconducting quantum processors with up to 95 qubits, leveraging advanced hardware optimization and readout error suppression. Building on these high-fidelity, large-scale entangled states, we investigated symmetry-protected topological phases in 1D linear cluster states and explored their robustness against symmetry perturbations. Our experiments revealed state-dependent sensitivity in teleportation fidelity, providing insights into the preservation of quantum information under symmetry-breaking influences. Looking ahead, further improvements in noise mitigation, hardware architecture, and error correction will be essential for scaling these results to even larger quantum systems. The insights gained from this work provide a solid foundation for realizing scalable measurement-based quantum computation and bringing us closer to unlocking the full potential of near-term quantum technologies.

ACKNOWLEDGMENTS

Funding: This research was supported by the Innovation Program for Quantum Science and Technology (Grant No. 2021ZD0300200, No. 2023ZD0300200), Anhui Initiative in Quantum Information Technologies, the Special funds from Jinan Science and Technology

Bureau and Jinan high tech Zone Management Committee, Shanghai Municipal Science and Technology Major Project (Grant No. 2019SHZDZX01), National Natural Science Foundation of China (Grants No. 92476203) and the New Cornerstone Science Foundation through the XPLOERER PRIZE. M. Gong was sponsored by National Natural Science Foundation of China (Grants No. T2322024), Shanghai Rising-Star Program (Grant No. 23QA1410000) and the Youth Innovation Promotion Association of CAS (Grant No. 2022460).

- [1] D. Azses, R. Haenel, Y. Naveh, R. Raussendorf, E. Sela, and E. G. Dalla Torre, *Phys. Rev. Lett.* **125**, 120502 (2020).
- [2] R. Raussendorf and H. J. Briegel, *Phys. Rev. Lett.* **86**, 5188 (2001).
- [3] R. Raussendorf, D. E. Browne, and H. J. Briegel, *Physical Review A* **68**, 022312 (2003).
- [4] S. Bravyi, S. Sheldon, A. Kandala, D. C. McKay, and J. M. Gambetta, *Phys. Rev. A* **103**, 042605 (2021).
- [5] M. A. Nielsen and I. L. Chuang, *Quantum Computation and Quantum Information*, 10th ed. (Cambridge University Press, 2010).
- [6] R. Horodecki, P. Horodecki, M. Horodecki, and K. Horodecki, *Reviews of Modern Physics* **81**, 865 (2009).
- [7] L. Amico, R. Fazio, A. Osterloh, and V. Vedral, *Reviews of Modern Physics* **80**, 517 (2008).
- [8] R. Jozsa, arXiv preprint quant-ph/9707034 (1997).
- [9] T. M. Graham, Y. Song, J. Scott, C. Poole, L. Phuttitarn, K. Jooya, P. Eichler, X. Jiang, A. Marra, B. Grinkemeyer, M. Kwon, M. Ebert, J. Cherek, M. T. Lichtman, M. Gillette, J. Gilbert, D. Bowman, T. Ballance, C. Campbell, E. D. Dahl, O. Crawford, N. S. Blunt, B. Rogers, T. Noel, and M. Saffman, *Nature* **602**, 63 (2022).
- [10] T. D. Ladd, F. Jelezko, R. Laflamme, Y. Nakamura, C. Monroe, and J. L. O'Brien, *Nature* **464**, 45 (2010).
- [11] X.-L. Wang, Y.-H. Luo, H.-L. Huang, M.-C. Chen, Z.-E. Su, C. Liu, C. Chen, W. Li, Y.-Q. Fang, X. Jiang, J. Zhang, L. Li, N.-L. Liu, C.-Y. Lu, and J.-W. Pan, *Physical Review Letters* **120**, 260502 (2018).
- [12] A. Omran, H. Levine, A. Keesling, G. Semeghini, T. T. Wang, S. Ebadi, H. Bernien, A. S. Zibrov, H. Pichler, S. Choi, J. Cui, M. Rossignolo, P. Rembold, S. Montangero, T. Calarco,

- M. Endres, M. Greiner, V. Vuletić, and M. D. Lukin, *Science* **365**, 570 (2019).
- [13] M. Gong, M.-C. Chen, Y. Zheng, S. Wang, C. Zha, H. Deng, Z. Yan, H. Rong, Y. Wu, S. Li, F. Chen, Y. Zhao, F. Liang, J. Lin, Y. Xu, C. Guo, L. Sun, A. D. Castellano, H. Wang, C. Peng, C.-Y. Lu, X. Zhu, and J.-W. Pan, *Physical Review Letters* **122**, 110501 (2019).
- [14] P. Thomas, L. Ruscio, O. Morin, and G. Rempe, *Nature* **608**, 677 (2022).
- [15] C. Song, K. Xu, H. Li, Y.-R. Zhang, X. Zhang, W. Liu, Q. Guo, Z. Wang, W. Ren, J. Hao, H. Feng, H. Fan, D. Zheng, D. Wang, H. Wang, and S. Zhu, *Science* **365**, 574 (2019).
- [16] H. Cao, L. M. Hansen, F. Giorgino, L. Carosini, P. Zahalka, F. Zilk, J. C. Loredó, and P. Walther, *Physical Review Letters* **132**, 130604 (2023).
- [17] M. Pont, G. Corrielli, A. Fyrrillas, I. Agresti, G. Carvacho, N. Maring, P.-E. Emeriau, F. Cacciarelli, R. Albiero, P. H. D. Ferreira, N. Somaschi, J. Senellart, I. Sagnes, M. Morassi, A. Lemaître, P. Senellart, F. Sciarrino, M. Liscidini, N. Belabas, and R. Osellame, *npj Quantum Information* **9**, 1 (2024).
- [18] S. Cao, B. Wu, F. Chen, M. Gong, Y. Wu, Y. Ye, C. Zha, H. Qian, C. Ying, S. Guo, *et al.*, *Nature* **619**, 738 (2023).
- [19] V. S. Ferreira, G. Kim, A. Butler, H. Pichler, and O. Painter, *Physical Review Letters* **129**, 260501 (2022).
- [20] S. Paesani and B. J. Brown, *Physical Review Letters* **131**, 120603 (2023).
- [21] Y. Guo and S. Yang, *npj Quantum Information* **9**, 11 (2023).
- [22] S. Krastanov, A. S. de la Cerda, and P. Narang, *Physical Review Research* **3**, 033164 (2021).
- [23] E. H. Chen, G.-Y. Zhu, R. Verresen, A. Seif, E. Bäumer, D. Layden, N. Tantivasadakarn, G. Zhu, S. Sheldon, A. Vishwanath, S. Trebst, and A. Kandala, *Nature Physics* (2024), 10.1038/s41567-024-02696-6.
- [24] Z. Bao, S. Xu, Z. Song, K. Wang, L. Xiang, Z. Zhu, J. Chen, F. Jin, X. Zhu, Y. Gao, Y. Wu, C. Zhang, N. Wang, Y. Zou, Z. Tan, A. Zhang, Z. Cui, F. Shen, J. Zhong, T. Li, J. Deng, X. Zhang, H. Dong, P. Zhang, Y.-R. Liu, L. Zhao, J. Hao, H. Li, Z. Wang, C. Song, Q. Guo, B. Huang, and H. Wang, *Nature Communications* **15**, 8823 (2024).
- [25] H. J. Briegel, D. E. Browne, W. Dür, R. Raussendorf, and M. V. den Nest, *Nature Physics* **5**, 19 (2009).
- [26] C. Greganti, M.-C. Roehsner, S. Barz, T. Morimae, and P. Walther, *New Journal of Physics* **18**, 013020 (2016).

- [27] R. R. Ferguson, L. Dellantonio, A. A. Balushi, K. Jansen, W. Dür, and C. A. Muschik, *Physical Review Letters* **126**, 220501 (2021).
- [28] P. Walther, K. J. Resch, T. Rudolph, E. Schenck, H. Weinfurter, V. Vedral, M. Aspelmeyer, and A. Zeilinger, *Nature* **434**, 169 (2005).
- [29] M. S. Tame, R. Prevedel, M. Paternostro, P. Böhi, M. S. Kim, and A. Zeilinger, *Physical Review Letters* **98**, 140501 (2007).
- [30] J. Wenner, R. Barends, R. Bialczak, Y. Chen, J. Kelly, E. Lucero, M. Mariantoni, A. Megrant, P. O'Malley, D. Sank, *et al.*, *Applied Physics Letters* **99** (2011).
- [31] E. Jeffrey, D. Sank, J. Mutus, T. White, J. Kelly, R. Barends, Y. Chen, Z. Chen, B. Chiaro, A. Dunsworth, *et al.*, *Physical review letters* **112**, 190504 (2014).
- [32] C. Macklin, K. O'brien, D. Hover, M. Schwartz, V. Bolkhovskiy, X. Zhang, W. Oliver, and I. Siddiqi, *Science* **350**, 307 (2015).
- [33] D. Paszko, D. C. Rose, M. H. Szymańska, and A. Pal, *PRX Quantum* **5**, 030304 (2024).
- [34] O. Gühne and G. Tóth, *Physics Reports* **474**, 1 (2009).
- [35] S. T. Flammia and Y.-K. Liu, *Physical Review Letters* **106**, 230501 (2011).
- [36] A. P. Place, L. V. Rodgers, P. Mundada, B. M. Smitham, M. Fitzpatrick, Z. Leng, A. Premkumar, J. Bryon, A. Vrajitoarea, S. Sussman, *et al.*, *Nature communications* **12**, 1779 (2021).
- [37] Y. Wu, W.-S. Bao, S. Cao, F. Chen, M.-C. Chen, X. Chen, T.-H. Chung, H. Deng, Y. Du, D. Fan, *et al.*, *Physical review letters* **127**, 180501 (2021).
- [38] D. V. Else, I. Schwarz, S. D. Bartlett, and A. C. Doherty, *Physical review letters* **108**, 240505 (2012).
- [39] R. Raussendorf, C. Okay, D.-S. Wang, D. T. Stephen, and H. P. Nautrup, *Physical review letters* **122**, 090501 (2019).
- [40] D. T. Stephen, D.-S. Wang, A. Prakash, T.-C. Wei, and R. Raussendorf, *Physical review letters* **119**, 010504 (2017).
- [41] F. Arute, K. Arya, R. Babbush, D. Bacon, J. C. Bardin, R. Barends, R. Biswas, S. Boixo, F. G. Brandao, D. A. Buell, *et al.*, *Nature* **574**, 505 (2019).
- [42] R. Raussendorf, D. E. Browne, and H. J. Briegel, *Physical review A* **68**, 022312 (2003).
- [43] D. Browne and H. Briegel, *Quantum information: From foundations to quantum technology applications*, 449 (2016).
- [44] M. A. Nielsen, *Reports on Mathematical Physics* **57**, 147 (2006).

SUPPLEMENTARY MATERIALS FOR “GENERATION OF 95-QUBIT GENUINE ENTANGLEMENT AND VERIFICATION OF SYMMETRY-PROTECTED TOPOLOGICAL PHASES”

Appendix A: Experimental system setup

Based on the *Zuchongzhi 2.0* quantum processor, we developed the *Zuchongzhi 3.1* processor with larger scale and improved performance by optimizing qubit topology design, materials, fabrication processes, and so on. The processor consists of 105 frequency-tunable transmon qubits and 182 tunable couplers, with the topology shown in Fig. S5, along with the qubits’ maximum frequencies, their idle T_1 times, readout frequencies, resonator linewidths κ_r , and coupling strengths between the qubits and resonators. The 105 qubits are divided into 15 rows for readout, each comprising seven qubits sharing a single readout Purcell filter.

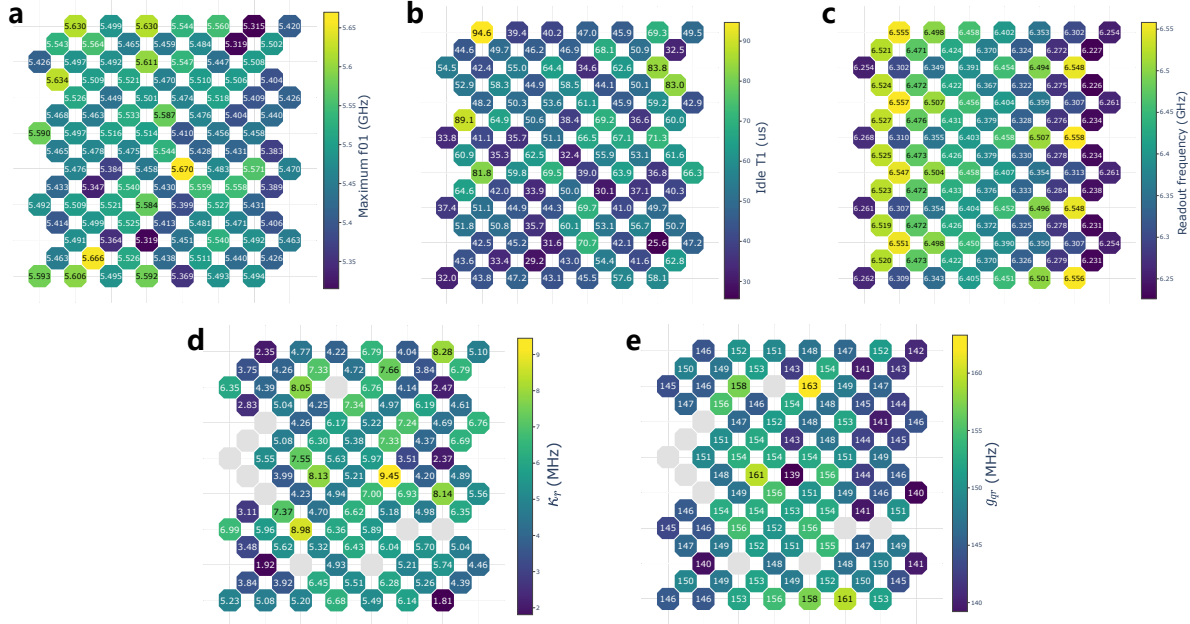


FIG. S5. Parameter distribution in the Processor. (a), (b) and (c) for 105 qubits. (a) Maximum frequency distribution. (b) Idle T_1 Distribution. (c) Readout frequency distribution. (d) and (e) for 95 qubits. (d) Resonator linewidth. (e) Qubit coupling to readout resonator.

We summarize the state and performance parameters of the processor, as detailed in Fig. S6. Compared to the *Zuchongzhi 2.0* processor, the enhancements in scale and perfor-

mance of the *Zuchongzhi 3.1* processor are attributed to the following improvements:

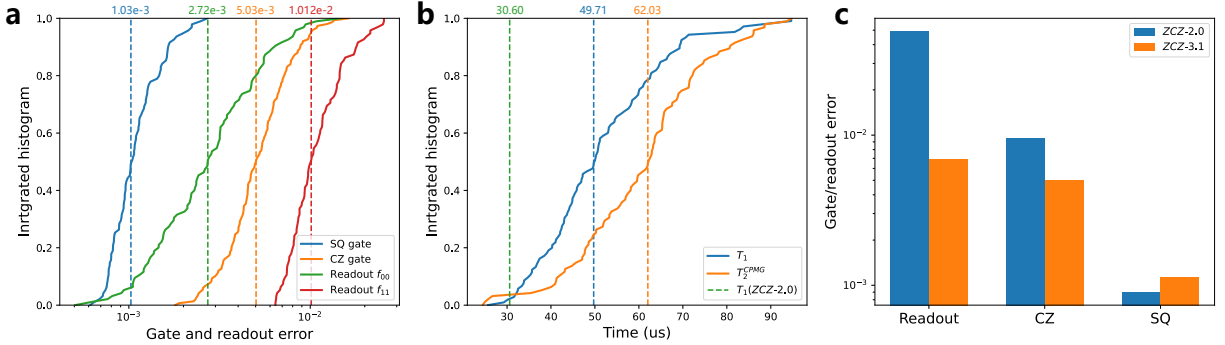


FIG. S6. Performance metrics for *Zuchongzhi 3.1* processor. (a) Integrated histograms of gate and measurement errors, showing error distributions for single-qubit(SQ) gate (0.103%), CZ gate (0.503%), and readout operations (f_{00} : 0.272%, f_{11} : 1.012%). SQ gates exhibit the lowest error rates, while CZ gates and measurement errors dominate overall error contributions. (b) Relaxation time T_1 (49.71 μs) and Carr-Purcell-Meiboom-Gill(CPMG) based coherence time T_2^{CPMG} (62.03 μs) for superconducting qubits, alongside the median T_1 of the *Zuchongzhi 2.0* device (30.60 μs). (c) Comparison of gate and measurement errors between two system configurations (*Zuchongzhi 2.0* and *Zuchongzhi 3.1*). *Zuchongzhi 3.1* (orange) demonstrates reduced errors for readout and CZ gate operations compared to *Zuchongzhi 2.0* (blue), indicating improved system performance. SQ gate errors remain consistently low across both systems.

Qubit design: In the design of the quantum processor, we first optimized the geometric dimensions of the qubits and couplers, reducing the electric field participation ratio (EPR) of them. The simulation results show that the surface dielectric loss of this processor is 1.6 times lower than that of the *Zuchongzhi 2.0* processor. While optimizing the geometric dimensions of the qubits, we also considered the requirements for scalable circuit design. In the current processor, the coupling between qubits consists of two components: direct capacitive coupling and indirect capacitive coupling. By tuning the frequency of the coupler between two qubits, the coupling strength can be quickly and precisely adjusted between approximately +3 MHz and -50 MHz. For the readout design, a multi-stage Purcell filter was implemented, which significantly suppresses the Purcell effect and enhances readout multiplexing and performance. Additionally, we optimized the coupling strength between the processor and external components, as well as the sample box design, further improving

the coherence and control performance of the processor.

Materials and fabrication process: The *Zuchongzhi 3.1* processor employs flip-chip bonding technology. The top chip contains only the qubits and couplers, while all readout and control lines are placed on the bottom chip. To suppress signal crosstalk, all control lines are covered with full-encapsulation crossovers. The readout transmission lines and resonators use isolated crossovers to suppress slotline modes. For both top and bottom chips, a high quality 200 nm α -tantalum thin film was fabricated on a sapphire substrate using magnetron sputtering. Before deposition, the sapphire substrate underwent piranha solution cleaning, followed by high-temperature annealing and deposition. On the high-quality α -tantalum thin film, the coplanar waveguide layer was fabricated using reactive ion etching (RIE). For the bottom chip, the crossover structure was prepared using a pattern transfer and deposition method to sequentially fabricate the silicon dioxide dielectric layer and aluminum bridges. For the top chip, the coupler and qubit Josephson junctions were fabricated using a double-angle evaporation technique. After indium bump deposition was completed on the top and bottom chips, the chips were diced, flip-chip bonded, and packaged.

Transmission system: After chip fabrication, the processor is connected and secured to a PCB in a gold-plated copper sample box by wire bonding. The fully packaged processor is then mounted on the MXC stage of a dilution refrigerator and connected to room-temperature electronics via microwave transmission lines. The experimental wiring setup for qubit and coupler controls and frequency-multiplexed readouts is shown in Fig. S7. To suppress thermal noise from room-temperature electronics, as well as signal attenuation and shielding, appropriate attenuators and low-pass filters are installed at different temperature stages of the dilution refrigerator. Compared to the signal system of the *Zuchongzhi 2.0* processor, we optimized the integration and thermal load of the signal transmission lines in this system. Additionally, in the readout chain, we replaced the Josephson parametric amplifier (JPA) with an in-house developed traveling wave parametric amplifier (TWPA) as the first-stage amplifier for readout signals, further enhancing the signal-to-noise ratio and multiplexing capability of the readout system.

Room-temperature electronics System: We designed and developed a high-integration room-temperature electronics system based on digital mixing and direct RF sampling, achieving an integration density of 10 qubits/Unit. The system uses a PXIE chassis as its foundational architecture and includes control modules, readout modules, communica-

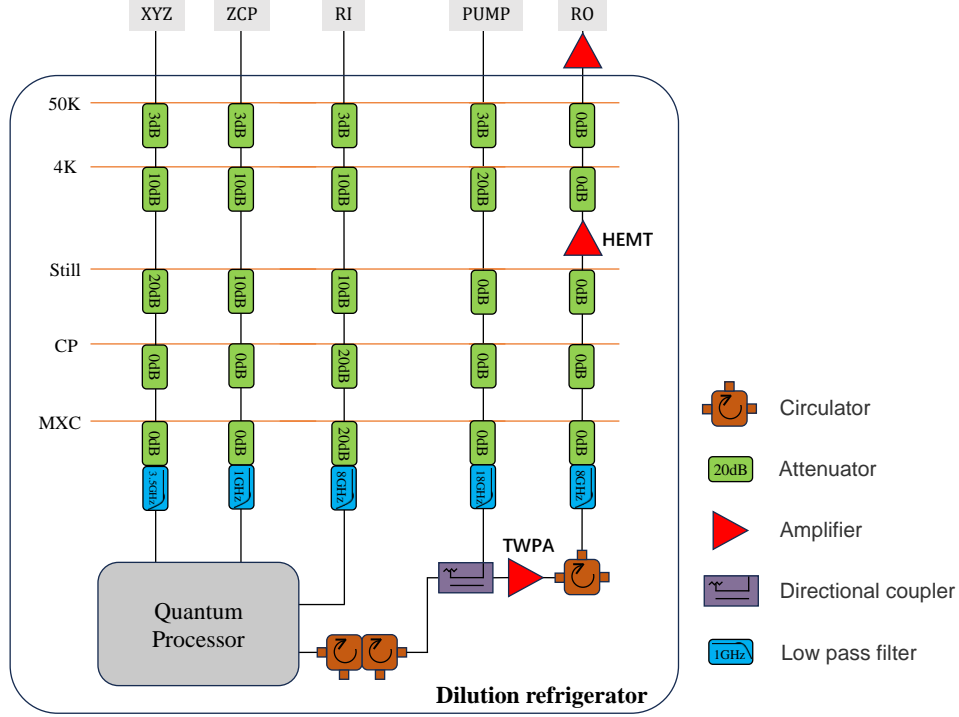


FIG. S7. The schematic diagram of control electronics and wiring in refrigerator. Each qubit has corresponding XY and Z control lines, which are combined at room temperature stage using a bias tee before entering the dilution refrigerator. Similarly, the control lines for couplers are independently routed into the refrigerator due to different filtering requirements. In the dilution refrigerator, attenuators and filters are installed at various stages to reduce noise. Traveling wave parametric amplifiers (TWPA), high electron mobility transistors (HEMT) and room-temperature amplifiers are used to amplify the readout signals. At room temperature, the integrated room-temperature electronics mentioned later provides XY/Z control signals as well as RI, RO, and Pump signals. Before being fed into the TWPA, the pump signal is combined with the chip's readout signal through a directional coupler. The readout signals amplified by the room-temperature amplifiers are digitized and demodulated by ADC modules.

tion modules, and support for multi-chassis synchronization and feedback cascading. As shown in the Fig. S8, the single chassis accommodates 16 control cards, 4 readout cards, 1 communication card, 1 system synchronization card, and 1 clock trigger synchronization card in its front and rear slots. The control module generates both XY signals and Z signals. Z signals are produced using a conventional 1 GSPS 4-channel DAC chip, while the XY signals are generated directly by an RF DAC chip. The 16 control cards offer 128

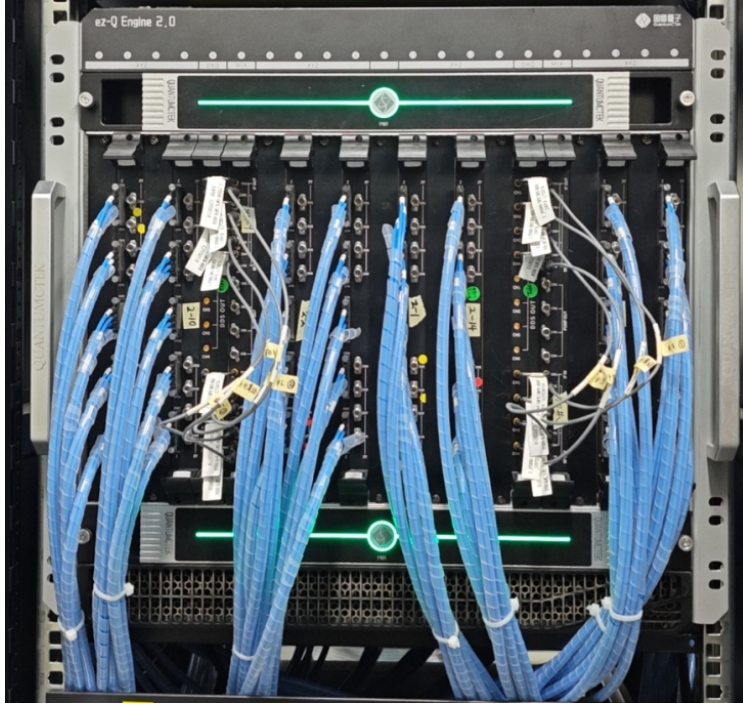


FIG. S8. The room-temperature electronics devices used in our experiment.

XY channels and 320 Z channels. Considering quantum chips with couplers, the control cards in a single chassis can manipulate at least 107 qubits. Besides, we have integrated digital quadrature modulator and NCO module in the RF DAC, so that issues such as signal leakage caused by analog IQ mixers are effectively avoided. Additionally, the high data rate of the high-sampling-rate chips utilizes the JESD 204B/204C standard, requiring only a minimal number of high-speed GT interfaces on the FPGA, which facilitates high integration. The readout module includes readout excitations, readout acquisitions, and readout pumps. Each of the 4 readout cards provides 8 RO, 8 RI, and 8 PUMP signals. The readout acquisition employs a single-sideband mixing scheme to reduce the usage of ADC/DAC channels, achieving a bandwidth of 1.8 GHz, which enables real-time demodulation of 16 qubit states. The readout excitation uses the same RF DAC scheme as the control XY signals, generating 1.8 GHz bandwidth signals that are upconverted through mixing to control the readout excitation of the qubits. The readout module also integrates PUMP signals that support 7–9 GHz and 12–14 GHz frequencies to meet the driving requirements of both TWPA and JPA.

In addition, we made corresponding improvements in noise control and electromagnetic

shielding. Through the optimizations and improvements mentioned above, the *Zuchongzhi 3.1* processor achieved the integration of 105 qubits and 182 couplers, totaling 287 transmons. This processor also demonstrated significant improvements in two-qubit gate fidelity and measurement performance.

Considering factors such as qubit measurement performance, coherence, and gate fidelity, we selected up to 95 qubits from the 105 operational qubits for our experiments based on the actual experimental requirements.

Appendix B: Processor calibration

The processor calibration process in superconducting quantum computing typically involves frequency arrangement strategy, single-qubit gate calibration, two-qubit gate calibration, and readout calibration. These steps are crucial for ensuring qubits can reliably perform quantum gate operations with precise and accurate readout. To enable large-scale cluster state preparation, we have developed a more efficient processor calibration process.

1. Frequency arrangement strategy

As the scale of superconducting quantum processors rapidly expands, determining how to effectively allocate the frequencies of qubits, couplers, and readout has become one of the key challenges in quantum processor measurement and control. The frequency arrangement strategy must take into account various factors, including direct and parasitic couplings, signal crosstalk, noise propagation, and so on.

Based on the error model of quantum gates, we developed a feasible frequency arrangement strategy to reduce errors during parallel gate operations, shown in Fig. S9a. In the quantum gate error model, the error model was instantiated using processor parameters and various error model functions. During the processor's initial calibration, we obtained state data from calibration experiments, including the qubit frequency-flux bias spectrum, qubit coherence performance and its frequency dependence, residual coupling parameters, distortion response parameters, XY signal crosstalk parameters, and other relevant data.

The error model functions were divided into two categories based on single-qubit gate Pauli errors and two-qubit gate Pauli errors. The single-qubit gate error model accounted for

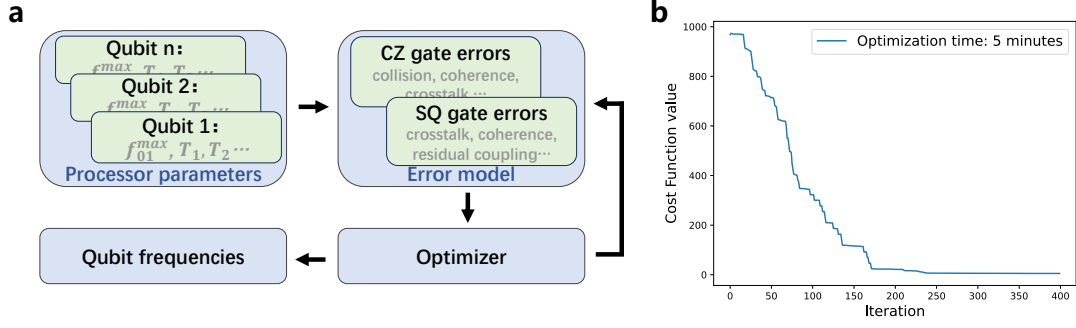


FIG. S9. Frequency arrangement strategy for reducing errors in parallel gate operations. (a) Flowchart illustrating Frequency arrangement strategy. (b) Error rate convergence curve of the frequency arrangement optimizer, demonstrating convergence within five minutes.

factors such as residual coupling during gate operation, qubit coherence performance, and XY signal crosstalk. The two-qubit gate error model function, specifically addressing CZ gate errors in this experiment, primarily considered frequency collisions along the qubit frequency trajectories during gate operation, coherence performance, and its frequency dependence, as well as crosstalk from signal distortion in the CZ gate.

Additionally, to comply with the requirements of our room-temperature electronics and ensure signal phase synchronization, we introduced supplementary frequency allocation rules to constrain the frequency optimization range.

After instantiating the error model, we define the optimizer's objective function:

$$CostFunction = Opt(Freqs, Patterns, Model) \quad (B1)$$

where *Freqs* is a one-dimensional frequency list containing the qubit idle frequencies and the CZ gate interaction frequencies, *Patterns* is a set of coupler groups, each used for the parallel execution of CZ gates in the quantum circuit, and *Model* is the instantiation based on the processor parameters and error model functions. The optimizer employed a commercial, closed-source tool based on a tree search metaheuristic for discrete space optimization.

To accelerate convergence and reduce the optimization space, we imposed tight constraints on the frequency arrangement, allowing each optimization cycle to converge within five minutes and yield a solution, shown in Fig. S9b. However, the objective function for frequency arrangement is highly non-convex and often exhibits multiple local optima. After performing several optimization iterations, we selected the arrangement with the lowest

error rate among the identified local optima as the final result.

2. Quantum gate optimization

In this experiment, we updated the quantum gate optimization strategy to achieve high-fidelity single-qubit and CZ gate operations at larger scales. Addressing signal crosstalk is essential for ensuring high-fidelity parallel operations. To mitigate this, we effectively reduced control signal crosstalk on the processor using a full-encapsulation crossover process. However, XY signal crosstalk is observed for certain qubits, particularly those with multiple control lines crossing beneath them.

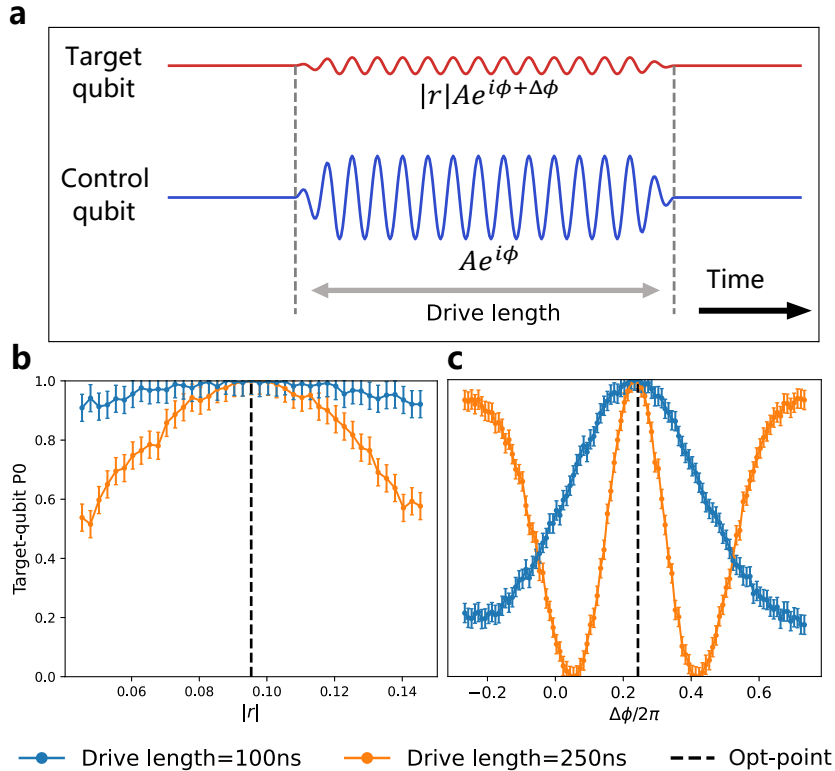


FIG. S10. Illustration of the active microwave crosstalk correction technology and the XY crosstalk calibration results. (a) Active microwave crosstalk correction applied to the affected qubits. (b) and (c) Calibration results showing the impact of microwave amplitude and phase adjustments on the target qubit. The blue line represents a drive length of $100ns$, while the orange line corresponds to a drive length of $250ns$.

To improve the fidelity of parallel single-qubit gates, we implemented active microwave

crosstalk correction technology, as illustrated in the Fig. S10a. Specifically, we apply a microwave signal with the same frequency and duration as the crosstalk signal to the affected qubits to mitigate its impact. The results from our XY crosstalk calibration experiment, also shown in the Fig. S10b and c, involve applying a drive signal of specific strength to the control qubit while systematically scanning the microwave amplitude and phase applied to the target qubit, enabling active compensation of the crosstalk waveform.

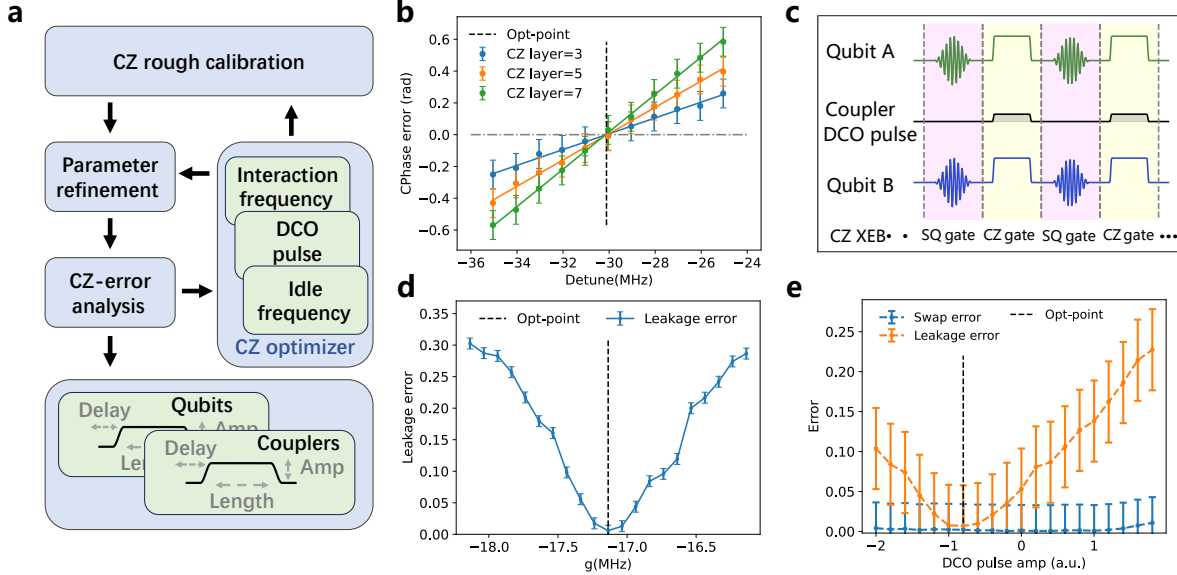


FIG. S11. CZ gate optimization. (a) Flowchart illustrating the CZ gate optimization strategy. (b) Dependence of c-phase error on the detuning parameter of the CZ gate, as obtained from the scan. (c) Schematic of the DCO technique, demonstrating the application of DCO pulses to couplers to mitigate re-coupling. (d) Dependence of leakage error on the coupling strength of the CZ gate coupler, as shown by the scan results. (e) Variation of swap and leakage errors during the DCO optimization, showing the change in error rates as a function of the coupling off point scan.

Prior to calibration, we had already determined a low-error-rate frequency arrangement based on the strategy outlined earlier, which included both idle and CZ interaction frequencies. Using this arrangement, we initially calibrated the CZ gate parameters and then performed distortion response calibration for the qubits and couplers during the CZ gate operation. To further ensure high-fidelity parallel CZ gate performance, we implemented an efficient calibration optimization procedure for the CZ parameters, as illustrated in the Fig. S11a, with the detailed process described as follows:

1. **Parameter refinement:** CZ gate errors were amplified using multi-layer CZ gate circuits, enabling precise optimization of qubit detuning frequencies and coupler coupling strengths. The optimization targeted cphase errors and leakage errors during CZ gate operations, shown in Fig. S11b and c.
2. **Interaction point optimization:** Signal crosstalk and frequency collisions in large-scale parallel CZ gate operations can significantly degrade the fidelity of certain gates. In this experiment, we not only targeted CZ SPB errors but also considered additional factors such as swap and leakage errors, which result from transitions of qubit states involving the $-1\rangle$ and $-2\rangle$ states of neighboring qubits. Two-qubit XEB [41] circuits were employed to optimize the CZ gate interaction frequencies, with a focus on minimizing these errors to improve overall gate fidelity.
3. **Local frequency adjustment:** The variation in TLS locations on the processor can introduce significant decoherence errors in the quantum gates of certain qubits. To mitigate this, we optimized the frequencies of the affected qubits and CZ gate interaction points. These adjustments, guided by the frequency arrangement model, aimed to reduce local coherence errors.
4. **Dynamic Coupling Off technology:** During CZ gate operations, qubit detuning can cause unintended re-coupling with neighboring qubits. To mitigate this, we introduced Dynamic Coupling Off(DCO) technology, applying DCO pulses of the same duration as the CZ gate waveform to couplers outside the pattern around the target qubit. The pulse amplitude was optimized to minimize swap and leakage errors involving transitions with the $-1\rangle$ and $-2\rangle$ states of neighboring qubits, shown in Fig. S11d and e, and the optimal coupling off point was selected based on these error metrics.

By employing the above optimization techniques, we achieved parallel CZ gates with a fidelity up to 99.50% and single-qubit gates with a fidelity exceeding 99.89% in this experiment.

3. Readout calibration

To achieve the preparation and witnessing of large-scale entangled states, it is crucial to simultaneously enhance parallel readout fidelities and minimize correlated measurement

errors. In superconducting quantum systems, readout operations are typically the most error-prone. As the processor scale increases, the issue of readout correlation errors caused by qubit frequency collisions, leading to state transitions and leakage, becomes more prominent. This effect becomes especially significant as readout fidelity improves, further amplifying the impact of correlation errors.

In this experiment, we integrated the model of readout correlation errors with experimental data to develop an efficient strategy for optimizing parallel readout. This approach combines theoretical insights and experimental findings to enhance parallel readout fidelity while minimizing correlation errors. The optimization process is as follows:

1. **Initial readout parameter calibration:** Determine the initial readout parameters, including frequency, amplitude, and length, based on dispersive shift and other readout calibration experiments.
2. **TWPA parameter optimization:** To determine the optimal operating point of the TWPA, the pump power and pump frequency are scanned to obtain the TWPA gain spectrum, as shown in Fig. S12a and b. Based on this spectrum, an optimal reference point is selected as the starting point for the optimization process. Subsequently, as shown in Fig. S12c, the NM algorithm is employed to maximize the signal-to-noise ratio (SNR) and fidelity of the readout, ultimately identifying the best operating point for the TWPA.
3. **Parallel readout optimization:** Readout parameters, such as power, length, and frequency, are optimized to maximize the fidelity of parallel qubit readout.
4. **Crosstalk readout optimization:** In superconducting quantum processors using dispersive readout, the AC Stark effect can induce qubit frequency shifts during readout, potentially causing frequency collisions and significant correlation readout errors as the processor scale increases. In the experiment, three representative circuits were selected for quick detection and, shown in Fig. S13a. By considering the weighted readout fidelity and differences among these circuits, parameters such as readout frequency, qubit frequency, and readout power were optimized, shown in Fig. S13b.
5. **Dynamic Coupling Off technology:** Qubit frequency shifts during readout can result in re-coupling, leading to readout correlation errors. To mitigate this, DCO

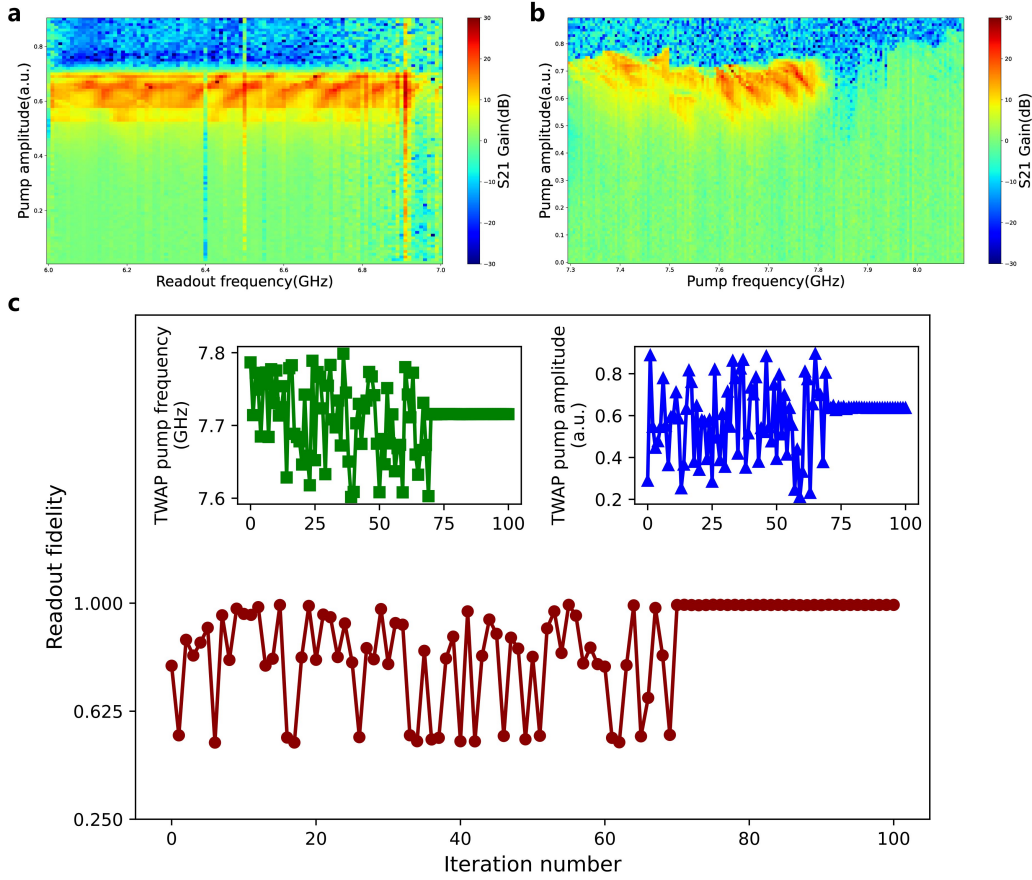


FIG. S12. Performance and optimization process of the traveling wave parametric amplifier (TWPA). (a) The TWPA gain spectrum with a fixed pump frequency 7.7 GHz, where the x-axis represents the readout frequency and the y-axis represents the pump amplitude. (b) The TWPA gain spectrum with a fixed readout frequency 6.55GHz, where the x-axis represents the pump frequency and the y-axis represents the pump amplitude. (c) Experimental data showing the optimization of the TWPA pump frequency and amplitude using the NM algorithm, with readout fidelity as the optimization target. The x-axis represents the number of iterations.

technology is also applied here, shown in Fig. S13c and d. By introducing a DCO waveform with the same duration as the readout waveform, coupling is dynamically turned off, thereby reducing readout correlation errors.

Through the optimization process described above, we reduced the readout errors to a level comparable to the two-qubit gate error rate, achieving a parallel O2 readout fidelity of up to 99.35%. The improvement in readout fidelity significantly enhanced our experimental

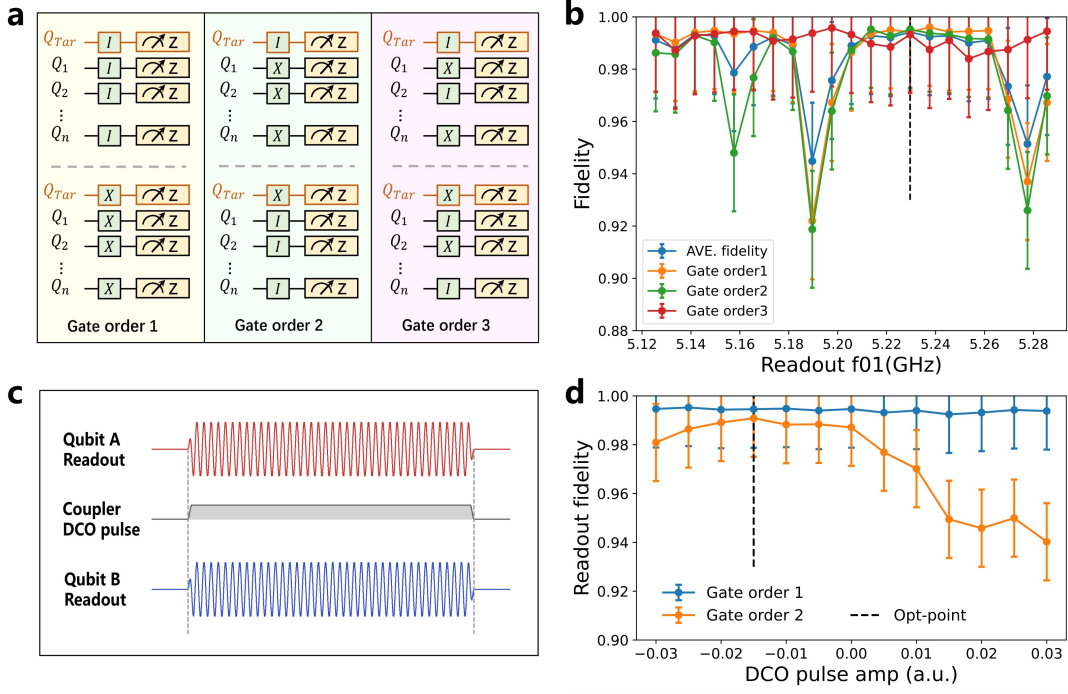


FIG. S13. Readout optimization. (a) Three representative circuits used for quick detection of readout correlation errors. (b) Experimental data showing the optimization of correlated readout by scanning the qubit frequency during readout. (c) Schematic of the DCO technique applied during readout. (d) Experimental data showing the results of the DCO parameter scan, demonstrating the reduction in readout correlation errors.

efficiency, enabling us to complete entanglement witness tasks with fewer random stabilizer circuits. In previous work, 4.3992×10^8 single measurements were required to estimate the fidelity of a 51-qubit cluster state. In contrast, in this experiment, only 1.0470×10^7 samples were needed to effectively estimate the fidelity of a 95-qubit cluster state, with a lower fidelity error.

Appendix C: Correlations of the measurement error

In this section, we will demonstrate that our processor exhibits very small measurement correlation errors. Experimentally, we characterize the correlated measurement error by covariance

$$\text{cov}[E_i, E_j] = \mathbb{E}[E_i \wedge E_j] - \mathbb{E}[E_i]\mathbb{E}[E_j], \quad (\text{C1})$$

where $E_{i(j)}$ denote the event that the measurement error appears in $Q_{i(j)}$, $E_i \wedge E_j$ denote the event of joint error with E_i and E_j .

Exepetiment	Number of qubits	Number of random satates	Number of repeat measure
1D cluster state	95	21500	3000
2D cluster state (sparse)	72	12200	3000
2D cluster state (full)	57	7200	3000

TABLE I. The numbers of random initial state and repeat measurement in our experiments for calibrated correlated error.

We calibrated the correlated measurement error by the random state preparation scheme [18]. The experiment parameters for characterizing correlated measurement errors in cluster state preparations are shown in Table I. For the 95Q 1D cluster state preparation experiment, we uniformly randomly generated 21,500 initial input states in $\{0, 1\}^{95}$, and independently repeated the measurement 3,000 times for each state. The results of the covariance for the measurement error of all qubit pairs are shown in Fig. S14a. According to the topological relationships of qubit pairs on the processor, which can be classified into three categories: adjacent pairs (coupled by couplers, a total of 150 pairs), share-readout-line pairs (with the same Purcell-filter and reading-signal line, a total of 257 pairs), and other non-local pairs (remaining cases, a total of 4,058 pairs). In Fig. S15, we present the proportion of qubit pairs with any type of covariance exceeding 0.1%, relative to the total number of measured pairs.

The experimental results indicate that the correlated measurement error mainly arises from adjacent pairs. This is because the AC-Stark effect of the readout waveform will cause a shift in qubit frequencies, leading to frequency collisions between qubits. Such collisions result in state leakage, which in turn introduces measurement correlation.

To further analyze the impact of correlated measurement errors on the experimental results, we presented the statistical distribution of two-qubit joint error and covariance from the random state preparation data of the one-dimensional cluster state preparation experiment, as shown in Fig. S16. The results show that the median covariance is at least one order less than the joint measurement error. Therefore, we can calculate the cluster state fidelity using the measurement error mitigation by the Tensor Product(TP) scheme while

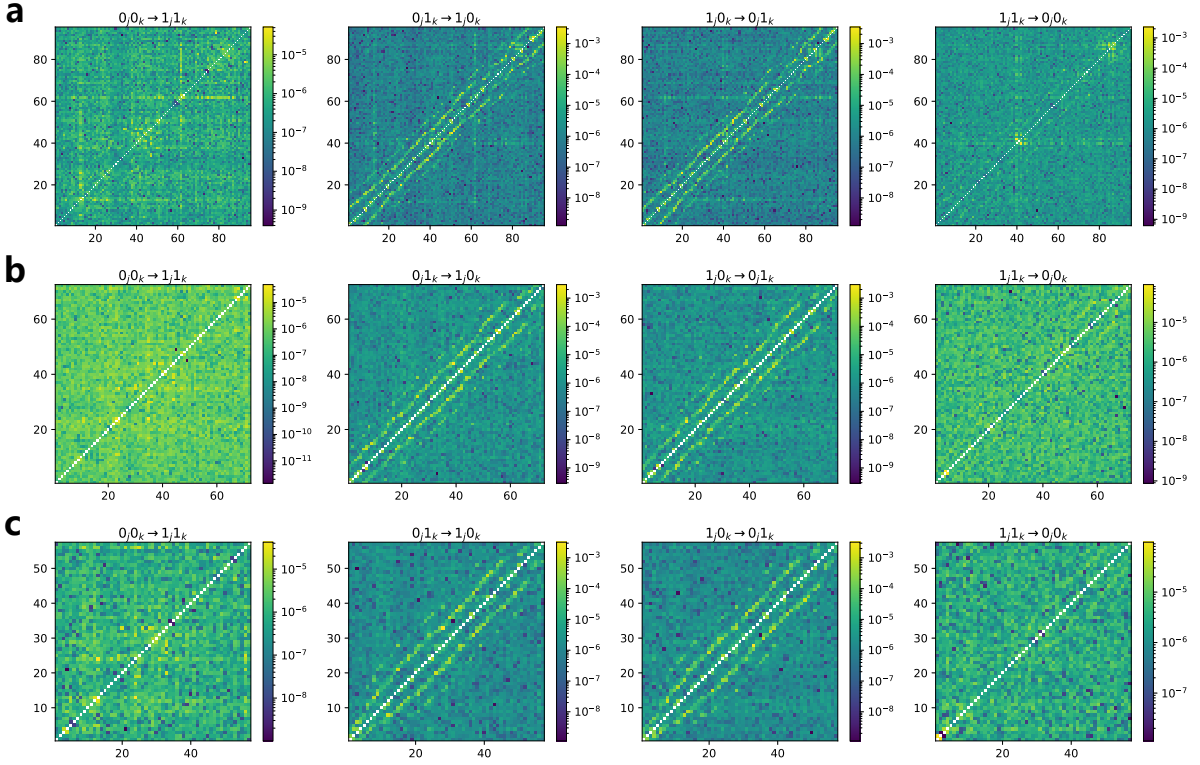


FIG. S14. The covariance of all flip errors for qubit pairs in (a) the 95Q 1D cluster state, (b) the 72Q sparse-2D cluster state, and (c) the 57Q full-2D cluster state. The $jk \rightarrow \bar{j}\bar{k}$ denotes the covariance of two qubits with input state $|j, k\rangle$ and output state $|\bar{j}, \bar{k}\rangle$.

neglecting the correlated measurement errors. Additionally, in the following chapters, we provide a more detailed discussion of the impact of correlated errors. For comparison, using the Continuous Time Markov Processes (CTMP) scheme, we present the cluster fidelity results obtained after considering the main correlated errors, which are consistent with the results by the tensor-product scheme.

Appendix D: Correction of measurement errors

1. Theoretical analysis

Measurement errors play a critical role in the accuracy of quantum device readout. Accurate calibration of these errors is crucial for improving the overall performance of quantum computations, particularly in enhancing fidelity and enabling reliable entanglement witness-

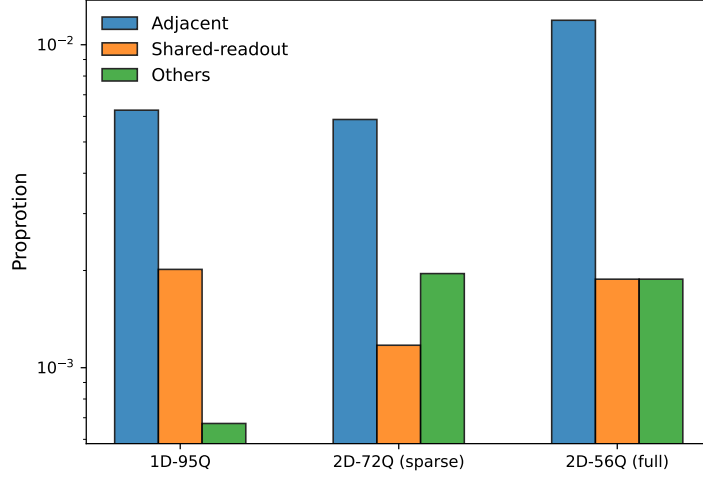


FIG. S15. Proportion of qubit pairs with covariance exceeding 0.1% across the three qubit pair categories: adjacent, shared-readout, and others. The proportions are calculated relative to the total number of measured pairs for each experiment.

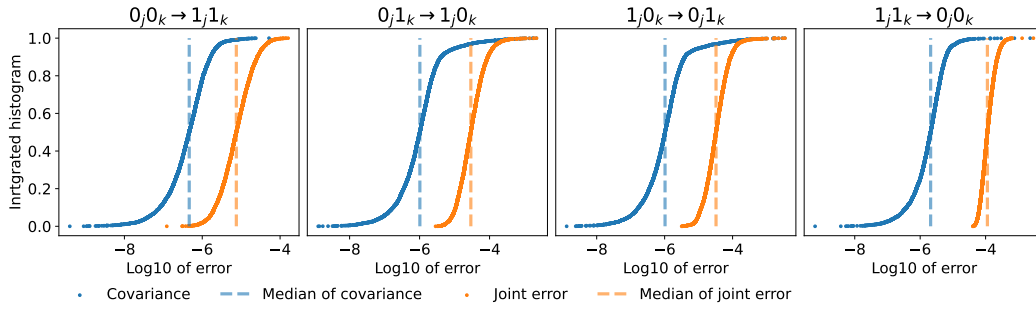


FIG. S16. Distribution of covariance and joint-error for the qubit pairs having the same device as 95Q 1D cluster state, where $jk \rightarrow \bar{j}\bar{k}$ denotes the covariance of two qubits with input state $|j, k\rangle$ and output state $|\bar{j}, \bar{k}\rangle$.

ing in cluster states.

In the absence of measurement errors, the estimation v can be obtained by aggregating the results of M distinct measurement settings P_i (on n qubits), with each setting being

repeated K times to gather sufficient statistics. The estimation formula for v is given by

$$v = \frac{1}{MK} \sum_{m=1}^M \text{sign}(P_m) \sum_{k=1}^K O(S_{mk}), \quad (\text{D1})$$

where S_{mk} denotes the outcome string obtained from the k -th repetition of the m -th measurement setting, and $O(S)$ is a function that maps the outcome string S to a scalar value. Specifically, $O(S)$ is defined as

$$O(S) = \prod_{i=1}^n \mu(s_i) := \prod_{i=1}^n (1 - 2s_i), \quad (\text{D2})$$

where s_i represents the binary outcome for the i -th qubit.

To account for the impact of readout errors, we introduce the $2^n \times 2^n$ readout noise matrix Λ , which represents the cumulative noise affecting the measurement outcomes of a quantum state. This matrix models the deviation between the ideal measurement outcomes and the actual, noisy observations. To correct for these deviations, we compute the inverse of the noise matrix, Λ^{-1} , and apply it to the observed measurement statistics. The calibrated estimation becomes

$$v_c = \frac{1}{MK} \sum_{m=1}^M \text{sign}(P_m) \sum_{k=1}^K \sum_x O(x) \langle x | \Lambda^{-1} | S_{mk} \rangle. \quad (\text{D3})$$

This process effectively “undoes” the influence of the readout noise, allowing us to recover a more accurate representation of the underlying quantum state.

The error in estimating the expectation of a random variable using the mean of a finite number of samples is governed by Hoeffding’s inequality. For a random variable v , which is the average of measured outcomes, Hoeffding’s inequality provides the following bound on the probability of deviation from the true expectation $\text{E}[v]$

$$\Pr(|v - \text{E}[v]| \geq \epsilon) \leq 2 \exp\left(-\frac{2N^2\epsilon^2}{\sum_{m=1}^N (b_m - a_m)^2}\right), \quad (\text{D4})$$

where $N = MK$ is the total number of measurements, and b_m and a_m are the upper and lower bounds of the m -th random variable, respectively. For our framework, the measurement outcomes are bounded between -1 and 1 , so $b_m = 1$ and $a_m = -1$. Substituting these bounds, the denominator simplifies to $4N$, and Hoeffding’s inequality becomes $\Pr(|v - \text{E}[v]| \geq \epsilon) \leq 2 \exp(-N\epsilon^2/2)$. To estimate the error ϵ with a confidence level of

$1 - \delta$, we solve for ϵ such that the probability of error is δ

$$\epsilon = \sqrt{\frac{2 \log(2/\delta)}{N}}. \quad (\text{D5})$$

Alternatively, for a desired error ϵ , the total number of measurements N required to achieve a confidence level $1 - \delta$ can be expressed as

$$N \geq \left\lceil \frac{2 \log(2/\delta)}{\epsilon^2} \right\rceil. \quad (\text{D6})$$

If we consider v as an average over M independent measurement settings, $v = \frac{1}{M} \sum_{m=1}^M \langle v_m \rangle$, where different repetitions of the operator v_i follows an identical distribution, the total number of measurements is distributed as $N = MK$. From Hoeffding's inequality, we can derive separate conditions on M and K

$$M \geq \left\lceil \frac{2 \log(2/\delta)}{\epsilon^2} \right\rceil, \quad (\text{D7})$$

and consequently, the number of repetitions K satisfies $K \geq 1$. This ensures that $N = MK$ meets the required conditions for error bounds.

Through a straightforward derivation, it becomes evident that the presence of bit-flip errors effectively reduces the average value of v . To counteract this influence, we apply the inverse of the noise operation, denoted as Λ^{-1} , which restores the original scale by ‘‘dilating’’ v back. However, this correction process introduces a trade-off: while it compensates for the shrinkage, it simultaneously broadens the range of the random variables, thereby amplifying the associated statistical uncertainty. As a result, the error in the final estimation increases, necessitating a higher number of measurements for accurate calibration. To formalize this intuition, we define the *overhead* of the error mitigation method as

$$\Gamma = \max_S \sum_x |\langle x | \Lambda^{-1} | S \rangle|. \quad (\text{D8})$$

This quantity measures the extent to which the error mitigation procedure amplifies the variance. Its impact on the error analysis modifies the bounds on the estimation error and the required sample size as follows

$$\epsilon = \Gamma \sqrt{\frac{2 \log(2/\delta)}{N}}, \quad N \geq \left\lceil \frac{2\Gamma^2 \log(2/\delta)}{\epsilon^2} \right\rceil. \quad (\text{D9})$$

Here, ϵ denotes the estimation error, δ the confidence interval, and N the number of measurements.

We further introduce the concept of *noise strength*, defined as

$$\gamma = - \min_{x \in \{0,1\}^n} \langle x | G | x \rangle, \quad (\text{D10})$$

where $G = \log(\Lambda)$. The relationship between Γ and γ is approximately given by $\Gamma \approx e^{2\gamma}$.

Due to the enormous size of Λ ($2^n \times 2^n$), we usually cannot compute it nor its inverse, which urges us to find a simpler model to decompose it into smaller subspaces. In this section, we explore two distinct noise models to address readout error mitigation: the qubit-independent noise model and the correlated Markovian noise model.

a. Qubit-independent noise calibration

Under the qubit-independent noise model, we assume that readout errors act independently on each qubit in the quantum system. This assumption is often valid for devices where noise sources, such as measurement crosstalk, are minimal or negligible. By treating each qubit's noise contribution as independent, the overall noise matrix Λ can be expressed as a tensor product of individual qubit noise matrices

$$\Lambda = \bigotimes_{i=1}^n \Lambda_i, \quad (\text{D11})$$

where Λ_i represents the noise matrix corresponding to the i -th qubit's readout process. Thus Each Λ_i is typically a 2×2 stochastic matrix,

$$\Lambda_i = \begin{bmatrix} p(0|0) & p(0|1) \\ p(1|0) & p(1|1) \end{bmatrix} := \begin{bmatrix} 1 - \epsilon_i & \eta_i \\ \epsilon_i & 1 - \eta_i \end{bmatrix}, \quad (\text{D12})$$

which captures the probabilities of correctly or incorrectly reading out the two computational basis states, $|0\rangle$ and $|1\rangle$.

The independence assumption significantly simplifies the calibration process by enabling the characterization of each qubit's readout noise independently. This decouples the calibration of individual qubits from the collective behavior of the entire system, thus beneficial for scalability. In practice, we prepare the quantum device with $2n^2$ randomly chosen 01-bit strings as input states, to gain insights into two-qubit crosstalk effects (though this model may not strictly require it). By repeating this process for preparing each initial state multiple

times and measuring the outcomes, we collect sufficient statistics to estimate the probabilities associated with each computational basis state on individual qubits. Specifically, we estimate the probabilities of state transitions (bit-flip errors) for each qubit as

$$\begin{aligned}\hat{\epsilon}_i &= \frac{\sum_{x,y} m(y,x) \langle 1|y_i\rangle \langle x_i|0\rangle}{\sum_{x,y} m(y,x) \langle x_i|0\rangle}, \\ \hat{\eta}_i &= \frac{\sum_{x,y} m(y,x) \langle 0|y_i\rangle \langle x_i|1\rangle}{\sum_{x,y} m(y,x) \langle x_i|1\rangle},\end{aligned}\tag{D13}$$

where $m(y,x)$ represents the number of occurrences of the measured output state y when the input state was x .

For the tensor product (TP) form matrix $\Lambda = \bigotimes \Lambda_i$, one of its key advantages is the ability to perform operations efficiently at the level of individual qubits. Specifically, the inverse of Λ can be computed directly as $\Lambda^{-1} = \bigotimes \Lambda_i^{-1}$, leveraging the independence of the qubits in the tensor product structure. This decomposition is particularly useful when addressing readout errors, as it allows for these errors to be mitigated independently for each qubit without requiring a computationally expensive inversion of the full matrix Λ . In this framework, each 2×2 sub-matrix Λ_i from Eq. (D12) has a well-defined analytical inverse given by

$$\hat{\Lambda}_i^{-1} = \frac{1}{1 - \hat{\epsilon}_i - \hat{\eta}_i} \begin{bmatrix} 1 - \hat{\eta}_i & -\hat{\eta}_i \\ -\hat{\epsilon}_i & 1 - \hat{\epsilon}_i \end{bmatrix},\tag{D14}$$

from the estimated probabilities of bit-flip errors derived from prior characterization of the measurement process. This explicit form enables an efficient correction of measurement errors, provided the condition $1 - \hat{\epsilon}_i - \hat{\eta}_i > 0$ is satisfied, which ensures the inverse matrix remains well-defined.

Substituting this correction into the calibrated estimation formula in Eq. (D3), and incorporating the tensor product structure as shown in Eq. (D11), we obtain

$$v_c = \frac{1}{MK} \sum_{m=1}^M \text{sign}(P_m) \sum_{k=1}^K \prod_{i=1}^n \sum_{x_i \in \{0,1\}} \mu(x_i) \langle x_i | \Lambda_i^{-1} | s_i \rangle.\tag{D15}$$

This expression highlights that the full 2^n -dimensional Hilbert space can be reconstructed by combining the n qubit-wise subspaces, enabling efficient computation in systems with large numbers of qubits.

Leveraging the inverse matrix provided in Eq. (D14), we derive the overhead and noise

strength as

$$\Gamma_{\text{TP}} = \prod_{i=1}^n \frac{1 + |\epsilon_i - \eta_i|}{1 - \epsilon_i - \eta_i}, \quad \gamma_{\text{TP}} = \sum_{i=1}^n \max\{\epsilon_i, \eta_i\}. \quad (\text{D16})$$

Here, ϵ_i and η_i represent the parameters characterizing the noise affecting the i -th qubit. These expressions illustrate the cumulative nature of noise effects in a system with n qubits. The computational complexity for estimating quantities governed by Eq. (D15) scales as $O(nMK) = O(n\epsilon^{-2}\Gamma_{\text{TP}}^2)$, or equivalently $O(n\epsilon^{-2}\exp(4\gamma_{\text{TP}}))$, where M and K are constants related to the algorithm's iterative structure.

b. Correlated Markovian noise calibration

Although the qubit-independent noise model is both economical and often sufficiently accurate, it fails to capture correlations between two-qubit interactions. Experimental evidence shows that the state-switching probability of a qubit is frequently influenced by the states of its neighboring qubits. This necessitates a more comprehensive model that accounts for such correlations.

To address this, Bravyi et al. [4] introduced a noise model incorporating two-qubit correlations within the framework of Continuous-Time Markov Processes (CTMP). This model provides a systematic way to include both one-qubit and two-qubit noise interactions.

The correlated Markovian noise model is mathematically defined as

$$\Lambda = \exp(G), \quad G = \sum_{i=1}^{2n^2} r_i G_i \quad (\text{D17})$$

where $\exp(G) = \sum_{\alpha=0}^{\infty} G^\alpha / \alpha!$ is the matrix exponential, r_i is the error rate coefficient which can be calibrated by system measurement outcomes, and G_i are noise generators that encompass various types of one-qubit and two-qubit bit-flip noise interactions. The complete set of generators G_i , along with their corresponding noise processes and multiplicities, is detailed in Table II, including single-qubit bit-flip errors and two-qubit correlated errors.

To describe the correlated readout error between the j -th and k -th qubits, we use a 4×4 matrix $\Lambda(j, k)$, defined as

$$\langle u | \Lambda(j, k) | v \rangle = \Pr [y_{j,k} = u \mid x_{j,k} = v, y_{-j,-k} = x_{-j,-k}], \quad (\text{D18})$$

where $u, v \in \{00, 01, 10, 11\}$, and $x_{j,k}$ represents the two-bit binary measurement outcomes

Generator G_i	Readout error	Number of G_k
$ 1\rangle\langle 0 _j - 0\rangle\langle 0 _j$	$0_j \rightarrow 1_j$	n
$ 0\rangle\langle 1 _j - 1\rangle\langle 1 _j$	$1_j \rightarrow 0_j$	n
$ 10\rangle\langle 01 _{jk} - 01\rangle\langle 01 _{jk}$	$01_{jk} \rightarrow 10_{jk}$	$n(n-1)/2$
$ 01\rangle\langle 10 _{jk} - 10\rangle\langle 10 _{jk}$	$10_{jk} \rightarrow 01_{jk}$	$n(n-1)/2$
$ 11\rangle\langle 00 _{jk} - 00\rangle\langle 00 _{jk}$	$00_{jk} \rightarrow 11_{jk}$	$n(n-1)/2$
$ 00\rangle\langle 11 _{jk} - 11\rangle\langle 11 _{jk}$	$11_{jk} \rightarrow 00_{jk}$	$n(n-1)/2$

TABLE II. One-qubit and two-qubit generators of correlated Markovian noise, where $j, k \in [n]$ and $j < k$. The total number of generators is $2n^2$.

for the (j, k) qubits, while $x_{-j, -k}$ represents the measurement outcomes for all other $n - 2$ qubits.

Given that the readout error rates r_i are small, we approximate the (j, k) -th term of G as:

$$\hat{G}(j, k) = \mathcal{P}(\log(\hat{\Lambda}(j, k))), \quad j < k, \quad (\text{D19})$$

where \mathcal{P} is a channel that maps all negative off-diagonal elements in the input matrix to zero, and \log denotes the matrix logarithm, with the branch chosen such that $\log(\hat{\Lambda}(j, k)) = 0$ if $\hat{\Lambda}(j, k) = I$. This approximation is not exact, as the matrix exponential and logarithm are usually affected by commutation. The higher-order terms arising from commutation are given by

$$\begin{aligned} \exp(G) &= \exp\left(\sum_{i=1}^{2n^2} r_i G_i\right) = \left(\prod_{i=1}^{2n^2} \exp(r_i G_i)\right) \cdot \exp(\text{higher-order commutators}) \\ &= \left(\prod_{j, k \in [n]} \exp[G(j, k)]\right) \cdot (1 + O(r^2)) \\ &= \left(\prod_{j, k \in [n]} I \otimes \cdots \tilde{\Lambda}(j, k) \cdots \otimes I\right) \cdot (1 + O(r^2)), \end{aligned}$$

where $r = \max_i r_i$. However, $\tilde{\Lambda}(j, k)$ is not equivalent to $\Lambda(j, k)$ due to residual commutation effects. The relationship between $\Lambda(j, k)$ and $\tilde{\Lambda}(j, k)$ can be expressed as

$$\Lambda(j, k) = \text{Tr}_{\{-j, -k\}} \left(\prod_{j, k \in [n]} I \otimes \cdots \tilde{\Lambda}(j, k) \cdots \otimes I \right)$$

where the partial trace removes all qubits except j and k . Because different $\tilde{\Lambda}(j, k)$ terms interact through the non-commutation, the resulting $\Lambda(j, k)$ depends on contributions from the broader system, and it becomes clear that using $\Lambda(j, k)$ to approximate $\tilde{\Lambda}(j, k)$ is inherently a first-order, linear approximation. Fortunately, the error rates are usually small enough to support our approximation.

To estimate the error rates and the stochastic matrix $\Lambda(j, k)$ associated with the quantum processor, we generate $2n^2$ randomly chosen 01-bit strings as input states. Each initial state is prepared and measured multiple times to obtain statistically robust results. This procedure ensures sufficient sampling across the Hilbert space for accurate characterization of the system's noise properties.

From the definition in Eq. (D18), the elements of the estimated stochastic matrix $\Lambda(j, k)$ can be expressed as

$$\langle u | \hat{\Lambda}(j, k) | v \rangle = \frac{\sum_{x,y} m(y, x) \langle w | y_{j,k} \rangle \langle x_{j,k} | v \rangle \langle x_{-j,-k} | y_{-j,-k} \rangle}{\sum_{x,y} m(y, x) \langle x_{j,k} | v \rangle \langle x_{-j,-k} | y_{-j,-k} \rangle}, \quad (\text{D20})$$

where $m(y, x)$ represents the number of counts of the measured output state y for a given input state x . This ratio quantifies the conditional probabilities governing the stochastic process for qubits j and k while marginalizing over the remaining $n - 2$ qubits. Here, $x_{j,k}$ and $y_{j,k}$ denote the states of the j -th and k -th qubits, while $x_{-j,-k}$ and $y_{-j,-k}$ capture the states of all other qubits.

Using Eq. (D19), we compute the two-qubit error rates r_i , which describe transitions between specific qubit-pair states. For instance, the rate for the $00_{jk} \rightarrow 11_{jk}$ transition is estimated as

$$\hat{r}(00_{jk} \rightarrow 11_{jk}) = \langle 11 | \hat{G}(j, k) | 00 \rangle,$$

where $\hat{G}(j, k)$ is the error generator matrix derived from the stochastic matrix $\hat{\Lambda}(j, k)$. Similarly, one-qubit error rates can be inferred by summing over contributions from the relative two-qubit terms across all pairs involving the qubit of interest. For example, the bit-flip error rate for the $0_j \rightarrow 1_j$ transition is given by

$$\hat{r}(0_j \rightarrow 1_j) = \frac{1}{2(n-1)} \sum_{k \neq j} \left(\langle 10 |_{jk} \hat{G}(j, k) | 00 \rangle_{jk} + \langle 11 |_{jk} \hat{G}(j, k) | 01 \rangle_{jk} \right).$$

Here, the factor $1/(2(n-1))$ normalizes the sum to account for all qubit pairs involving qubit j .

After calibrating the elements of the stochastic matrices, we are ready to compute the inverse of Λ . As detailed in Eq. (D17), the inverse is related to the generator G through the matrix exponential, and using the decomposition $Q = I + \gamma^{-1}G$, we can rewrite Λ^{-1} as

$$\begin{aligned}\Lambda^{-1} &= \exp(-G) = \exp(\gamma I - \gamma Q) \\ &= \exp(\gamma) \sum_{\alpha=0}^{\infty} \frac{(-\gamma)^{\alpha} Q^{\alpha}}{\alpha!}.\end{aligned}\tag{D21}$$

where the parameter $\gamma = -\min_{x \in \{0,1\}^n} \langle x | G | x \rangle$. Interestingly, γ can be viewed as a classical Ising-like Hamiltonian with two-spin interactions. Heuristic methods such as simulated annealing or genetic algorithms can provide effective solutions in practice.

Instead of explicitly summing infinite terms in the series expansion, we propose a sampling-based method to estimate Λ^{-1} . From Eq. (D21), the inverse matrix can be expressed as

$$\Lambda^{-1} = \sum_{\alpha=0}^{\infty} c_{\alpha} S_{\alpha},$$

where

$$c_{\alpha} = \frac{e^{\gamma} (-\gamma)^{\alpha}}{\alpha!}, \quad S_{\alpha} = Q^{\alpha}.\tag{D22}$$

The coefficients c_{α} correspond to the terms in a weighted sum, and the normalization coefficient Γ is given by

$$\Gamma = \sum_{\alpha=0}^{\infty} |c_{\alpha}| = \sum_{\alpha=0}^{\infty} \frac{e^{\gamma} \gamma^{\alpha}}{\alpha!} = e^{2\gamma}.\tag{D23}$$

Thus, we can rewrite Λ^{-1} as

$$\Lambda^{-1} = \Gamma \sum_{\alpha=0}^{\infty} q_{\alpha} Q^{\alpha},\tag{D24}$$

where $q_{\alpha} = c_{\alpha}/\Gamma = \frac{e^{-\gamma} (-\gamma)^{\alpha}}{\alpha!}$. Notably, q_{α} follows a Poisson distribution with mean γ .

Thanks to this structure, we can efficiently approximate Λ^{-1} through sampling:

1. Sample α : Draw α from the Poisson distribution q_{α} .
2. Apply Q^{α} : Iteratively apply the matrix Q^{α} to the measurement outcomes $|S\rangle$.

In the second step, the matrix $Q = I + \gamma^{-1}G$ can be interpreted as a Markovian transfer matrix. Applying Q^{α} to the measurement outcomes $|S\rangle$ corresponds to performing a random

walk with Q for α steps. Since Q is a large, potentially non-local matrix, we can further decompose it as

$$Q = I + \gamma^{-1} \sum_{j,k} G(j, k).$$

For each step of the random walk, we randomly sample from the components of Q , selecting either I or $G(j, k)$ with probabilities proportional to their contributions in the decomposition. For α steps, we sequentially apply the sampled components G_{r_j} to the state $|S\rangle$. This decomposition reduces the complexity of handling the full matrix Q , and also allows us to make good use of the estimates in Eq. (D19).

Repeating the above sampling procedure T times, we calculate the calibrated estimation for M measurement settings and K repetitions as

$$\begin{aligned} v_c &= \frac{1}{MK} \sum_{i=1}^M \text{sign}(P_i) \sum_{k=1}^K \sum_x O(x) \langle x | \Lambda^{-1} | S_{ik} \rangle \\ &= \frac{\Gamma}{MKT} \sum_{i=1}^M \text{sign}(P_i) \sum_{k=1}^K \sum_{t=1}^T \sum_x O(x) \langle x | \prod_{j=1}^{\alpha_t} G_{r_j} | S_{ik} \rangle. \end{aligned} \quad (\text{D25})$$

Here, Γ serves as a normalization coefficient that effectively scales every outcome, reflecting the overhead introduced by the error mitigation method. This expression uses the sampled α_t and the corresponding matrix sequence $\prod_{j=1}^{\alpha_t} G_{r_j}$ to approximate the application of Λ^{-1} on the measurement outcomes. By averaging over T independent trials, the estimator converges to the calibrated value of v_c .

The noise strength γ_{CTMP} is determined via classical search algorithms. Using Eq.(D23), the overhead is expressed as

$$\Gamma_{\text{CTMP}} = \exp(2\gamma_{\text{CTMP}}). \quad (\text{D26})$$

The computational complexity for evaluating Eq. (D25) is given by $O(n\gamma_{\text{CTMP}}MKT) = O(n\epsilon^{-2}\gamma_{\text{CTMP}}\Gamma_{\text{CTMP}}^2)$, or equivalently $O(n\epsilon^{-2}\gamma_{\text{CTMP}}\exp(4\gamma_{\text{CTMP}}))$.

Upon careful examination, we observed that the CTMP overhead for the 1D 95-qubit cluster state becomes prohibitively large, leading to an impractically high number of required measurements. To address this issue, we propose customizing the summation set G in Eq. (D17), allowing for greater flexibility in the CTMP method. The method can be tailored as follows:

1. When the summation is restricted to single-qubit generators, the CTMP method reduces to the TP method, as no multi-qubit correlations are included.

2. If only nearest-neighbor two-qubit bit-flip noise is considered, the computational overhead is significantly reduced, making the approach more practical for large-scale systems.
3. Including all two-qubit correlations across the system enables the method to capture a broader range of correlated errors.
4. By calculating the two-qubit correlation coefficients for all bit-flip errors, defined as

$$r(E_1, E_2) = \frac{\text{cov}(E_1, E_2)}{\sqrt{\text{Var}(E_1)\text{Var}(E_2)}}, \quad (\text{D27})$$

where $\text{cov}(E_1, E_2) = \mathbb{E}(E_1, E_2) - \mathbb{E}(E_1)\mathbb{E}(E_2)$, $\text{Var}(E_1) = \mathbb{E}(E_1^2) - \mathbb{E}(E_1)^2$, we can identify qubit pairs with coefficients exceeding a threshold of 0.3 and selectively include them in the summation.

The table below compares the relative noise strength (γ), overhead (Γ), and total number of measurements needed in 1D 95-qubit cluster case for the TP model, single-qubit CTMP model, nearest-neighbor CTMP model, full 2-qubit correlation CTMP model and most-correlated CTMP model.

	TP		CTMP		
	TP	TP	nearest-neighbor	full-correlation	most-correlated
noise strength (γ)	0.96559	0.95877	2.8609	91.093	1.7161
overhead (Γ)	6.8976	6.8042	305.44	1.3266×10^{79}	30.945
number of measurements	7.2326×10^6	7.0381×10^6	1.4183×10^{10}	2.6752×10^{163}	1.4557×10^8

TABLE III. Comparison of TP and CTMP results.

The results are presented in the Table. III highlights the trade-offs between error suppression performance and computational resources for different noise-mitigation methods. The most correlated configuration offers a more balanced solution. By selecting qubit pairs with correlation coefficients above a threshold (e.g., 0.3), the method efficiently suppresses significant correlated errors without excessive resource overhead. We thus use this most correlated configuration in the following numerical simulations for CTMP models.

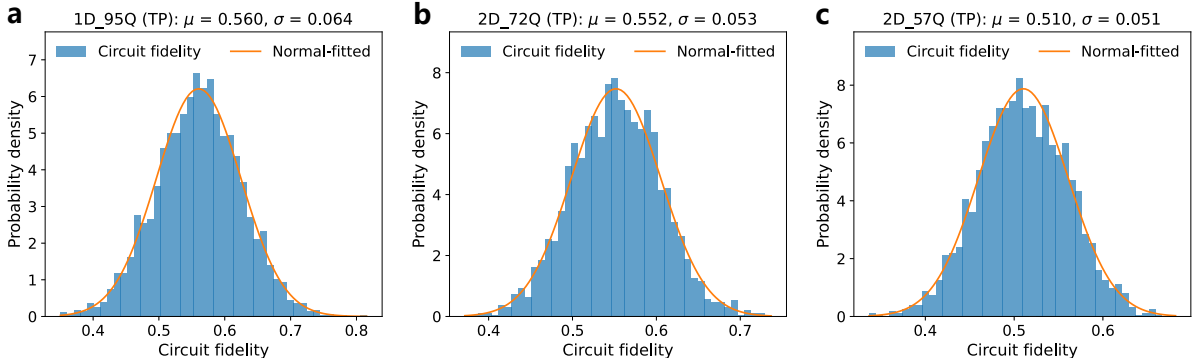


FIG. S17. Circuit fidelity distribution of 1D 95-qubit, 2D sparse 72-qubit and 2D full 57-qubit cases by TP method.

2. Experimental results

We numerically compute the Tensor Product (TP) error-mitigated fidelity and its associated error for 1D and 2D cluster states, scaling up to 95 qubits, 72 qubits (3-pattern), and 57 qubits (4-pattern), respectively. These results are summarized in the figures below, demonstrating the scalability and effectiveness of our error mitigation approach. The main text presents the TP error-mitigated results for both 1D and 2D cluster states. Beyond the theoretical bounds derived from error analysis, we also analyze the distribution of the average values for each measurement setting in the 1D 95-qubit, 2D 72-qubit, and 2D 57-qubit cases. This distribution provides insight into the variability across measurement outcomes and the reliability of the mitigated fidelity. Specifically, the variance across circuits for the 1D 95-qubit and 2D 72-qubit and 57-qubit cases is computed as $\sqrt{\text{Var}(\bar{v})} = 0.064, 0.053, 0.051$, respectively, as shown in Fig. S17. The relative variance of the total average estimation, given by $\epsilon = \sqrt{\text{Var}(\bar{v})/M}$, serves as an empirical estimate of fidelity error, yielding values of 0.00108, 0.00108, 0.00114, where M represents the total number of circuits.

To mitigate fidelity errors for 1D and 2D cluster states, we also employ the Continuous-Time Markov Processes (CTMP) model. A comparison of the CTMP and TP methods is presented in Fig. S18. While the CTMP model considers the most-correlated qubit pairs to reduce the overhead compared to the full CTMP approach, the improvement in fidelity is marginal, and the required number of measurements remains significantly higher. These observations support the adoption of the Tensor Product method in the main text as a

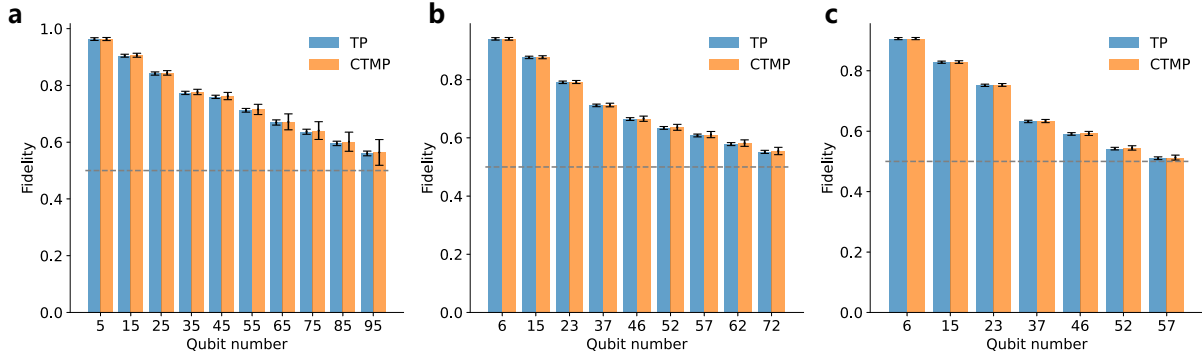


FIG. S18. Comparison of fidelity between the TP and CTMP methods for 1D and 2D cluster states with varying qubit numbers. The error-mitigated fidelity and corresponding error bars are plotted against the number of qubits in the cluster state. Here we use the most correlated CTMP configuration, selecting qubit pairs with correlation coefficients greater than 0.3. For the 1D 95-qubit cluster state, the TP method achieves a fidelity of 0.5603 ± 0.0084 , while the CTMP method reaches 0.5639 ± 0.0453 . For the 2D 72-qubit 3-pattern case, the TP method yields a fidelity of 0.5519 ± 0.0054 , compared to 0.5549 ± 0.0127 for the CTMP method. Similarly, for the 2D 57-qubit 4-pattern case, the TP method achieves a fidelity of 0.5104 ± 0.0045 , while the CTMP method reaches 0.5128 ± 0.0082 . All fidelity values are reported with 99.7% confidence. This figure is identical to Fig. 3 (d, e, f) in the main text.

more practical alternative. In addition to the error analysis, we present the distribution of average values for each measurement setting, as shown in Fig. S19. For 1D 95-qubit, 2D 72-qubit, and 2D 57-qubit cluster states, the variance across circuits in this scenario is computed as $\sqrt{\text{Var}(\bar{v})} = 0.118, 0.059, 0.053$. The relative variance of the total average estimation is $\epsilon = \sqrt{\text{Var}(\bar{v})/M} = 0.00200, 0.00121, 0.00118$, where M is the total number of circuits, serving as an empirical estimate of the fidelity error.

Appendix E: Simulation of Symmetry-Protected Topological Phases

We discuss the simulation of symmetry-protected topological (SPT) phases by preparing a family of SPT states that are adiabatically connected to the cluster state. We then detect the SPT order based on the measurement-based wire protocol as proposed in Ref. [1]. We introduce the cluster states as SPT states, the detection protocol, ways to tailor the protocol

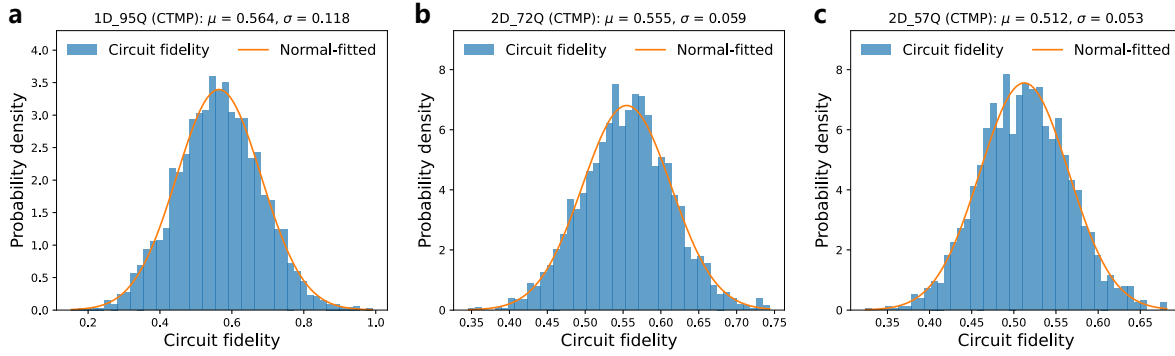


FIG. S19. Circuit fidelity distribution of 1D 95-qubit, 2D sparse 72-qubit and 2D full 57-qubit cases by CTMP method.

for compatibility with our experimental devices, and readout error mitigation for the method.

1. Cluster states as symmetry-protected topological states

In this section, we analyze the symmetry-protected topological (SPT) characteristics of cluster states. Cluster states are widely recognized as the ground states of a specific parent Hamiltonian defined as

$$H = - \sum_i h_i = - \sum_j X_j \prod_{k \in \mathcal{N}_j} Z_k, \quad (\text{E1})$$

where X and Z are Pauli operators acting on the respective qubits, and \mathcal{N}_j denotes the set of neighbors of qubit j . It is straightforward to verify that this Hamiltonian is the negative sum of the stabilizers of the cluster state. This parent Hamiltonian exhibits several key properties:

1. All terms in H commute with each other.
2. The Hamiltonian is gapped, with an integer-valued spectrum.
3. The cluster state is the unique ground state of H .

The SPT nature of the 1D cluster state arises from its invariance under a specific symmetry group, $\mathbb{Z}_2 \times \mathbb{Z}_2$. This symmetry group corresponds to the conservation of the parity of all

odd and even qubits, as defined by the operators

$$\begin{aligned}
 P_{\text{odd}} &= \prod_i h_{2i+1} = \prod_i X_{2i+1}, \\
 P_{\text{even}} &= \prod_i h_{2i} = \prod_i X_{2i}.
 \end{aligned}
 \tag{E2}$$

These symmetries ensure that the 1D cluster state remains within the same SPT phase under perturbations that respect $\mathbb{Z}_2 \times \mathbb{Z}_2$.

The cluster state's SPT nature is central to its robustness. Specifically, the entanglement structure persists under perturbations or noise that do not break the protecting symmetries. This robustness is particularly relevant in quantum information processing, where imperfections in hardware could otherwise destabilize the state. A defining feature of the non-trivial topology of the cluster state is the presence of symmetry-protected edge states. When a one-dimensional (1D) cluster chain is truncated, the edges of the chain host qubits that exhibit degenerate eigenstates are protected by the system's symmetries [1, 38]. These edge states serve as a clear indicator of the underlying topological order and play a critical role in the cluster state's suitability for measurement-based quantum computation.

2. Measurement-based wire protocol

It is known that the cluster state as a prototypical SPT state can serve as a computational resource for measurement-based quantum computing (MBQC). While the cluster state can only achieve universal MBQC in two dimensions, the cluster state can synthesize arbitrary $SU(2)$ operations. This includes the identity gate: An input state $|\psi_{\text{in}}\rangle$ is entangled with a n -qubit 1D cluster state chain by a control- Z gate and by measuring the input and first $(n - 1)$ qubits of the cluster state in the X basis, we get the last output qubit in the state $|\psi_{\text{out}}\rangle$. This process is illustrated in the main text Fig. 4A. A final correction unitary U_Σ is applied so that

$$|\psi_{\text{in}}\rangle = U_\Sigma |\psi_{\text{out}}\rangle. \tag{E3}$$

This emphasizes that the identity gate is not a null operation but a quantum teleportation of the input state. Similar to the textbook quantum teleportation protocol, the correction unitary U_Σ of the identity gate depends on the measurement results of the first n qubits.

It is known that the family of states possessing the same SPT order can all serve as resource states for MBQC. As such, as long as the $\mathbb{Z}_2 \times \mathbb{Z}_2$ symmetry is preserved, one

can implement basic MBQC operations leveraging the state, such as the identity gate. This provides us with a method for detecting the SPT order by whether the quantum teleportation is faithfully implemented, independent of the input state. As such, the scheme following Ref. [1] is to introduce two sets of unitaries acting on the cluster state:

$$\begin{aligned} U_S(\alpha, \beta) &= e^{i\beta Z_1 X_2 Z_3} e^{i\alpha X_3}, \\ U_{SB}(\alpha, \beta) &= e^{i\beta Z_1 X_2 Z_3} e^{i\alpha Y_3}. \end{aligned} \tag{E4}$$

One can readily check that $U_S(\alpha, \beta)$ and $U_{SB}(\alpha, \beta)$ preserves and breaks the $\mathbb{Z}_2 \times \mathbb{Z}_2$ symmetry. We also introduce $k = 2, 3, 4, 5, 6$ parallel implementations of the unitaries as shown in Fig. S21. For $k = 2$, the set of symmetry-preserving and breaking unitaries is

$$\begin{aligned} U_S(\alpha, \beta) &= e^{i\beta Z_1 X_2 Z_3} e^{i\alpha X_3} e^{i\beta Z_5 X_6 Z_7} e^{i\alpha X_7}, \\ U_{SB}(\alpha, \beta) &= e^{i\beta Z_1 X_2 Z_3} e^{i\alpha Y_3} e^{i\beta Z_5 X_6 Z_7} e^{i\alpha Y_7}. \end{aligned} \tag{E5}$$

For larger k , the setting is similar, such that a one-qubit interval is set between each unitary. The presence of the topological order of the resource states $U_S |\text{CL}\rangle$ or $U_{SB} |\text{CL}\rangle$ are then determined by the fidelity of the teleported states. To compute the fidelity, one first applies the correction unitary U_Σ and estimates the fidelity with the input state:

$$\mathcal{F}(|\psi_{\text{in}}\rangle \langle \psi_{\text{in}}|, \rho'_{\text{out}}) = \langle \psi_{\text{in}} | \rho'_{\text{out}} | \psi_{\text{in}} \rangle, \tag{E6}$$

where $\rho'_{\text{out}} = U_\Sigma \rho_{\text{out}} U_\Sigma^\dagger$. This density matrix can be estimated through single-qubit tomography, i.e. measuring in the Pauli basis: $\rho'_{\text{out}} = (1 + \langle X_{\text{out}} \rangle \sigma^x + \langle Y_{\text{out}} \rangle \sigma^y + \langle Z_{\text{out}} \rangle \sigma^z) / 2$. Yet, we find the computational process unamenable to our quantum device as feedforward quantum operations are unavailable. Therefore, a possible solution may be to postselect on the measurement results such that the set of ideal ρ_{out} is identical, i.e. have the same corresponding correction unitary. In the next section, we describe an even better scheme that exempts us from postselection.

3. Postselection-free fidelity estimation

In principle, feedforward quantum operations in MBQC protocols are necessary to successfully implement specific quantum gates. Yet, when the input state is a stabilizer state, we can circumvent this problem. This is in parallel with the fact that the MBQC protocol can implement Clifford circuits in a single round of measurement without feedforward operations.

Consider a single qubit stabilizer state $|\psi_{\text{in}}\rangle = C_{\text{in}}|0\rangle$ with stabilizer P_{in} , where C_{in} is a Clifford operation. Our protocol works by the following.

1. Entangle the input state with the n -qubit cluster state with a control-Z gate.
2. Measure the first n qubits in the Pauli X basis. For $n \in \mathbb{Z}_{\text{even}}$, measure for the last qubit in the $\{C_{\text{in}}|0\rangle, C_{\text{in}}|1\rangle\}$ basis by acting the C_{in} gate before the standard basis measurement. Otherwise, measure for the last qubit in the $\{HC_{\text{in}}|0\rangle, HC_{\text{in}}|1\rangle\}$ basis, where H is the Hadamard gate.
3. Denote the measurement outcome for the first n qubits as \mathbf{s} and the measurement outcome of the last qubit as $|i\rangle$. The one-shot fidelity is computed as

$$\mathcal{F}(\rho_{\text{in}}, \rho_{\text{out}}) = (-1)^a \langle i| C_{\text{in}} P_{\text{in}} C_{\text{in}}^\dagger |i\rangle \quad (\text{E7})$$

where a is determined by the commutation relationship between P_{in} and U_Σ such that $P_{\text{in}} U_\Sigma = (-1)^a U_\Sigma P_{\text{in}}$. The correction unitary is given by

$$U_\Sigma = Z^{s_{\text{even}} + s_0} X^{s_{\text{odd}}},$$

where $s_{\text{even}} = \sum_{i=1, i \in \mathbb{Z}_{\text{even}}}^n \mathbf{s}_i$ and $s_{\text{odd}} = \sum_{i=1, i \in \mathbb{Z}_{\text{odd}}}^n \mathbf{s}_i$.

4. Repeat Steps (1)-(3) sufficient times and take the empirical mean of the single-shot fidelities to get the final fidelity estimation, i.e., $\bar{\mathcal{F}}(\rho_{\text{in}}, \rho_{\text{out}}) = \frac{1}{M} \sum_{i=1}^M \mathcal{F}_i(\rho_{\text{in}}, \rho_{\text{out}})$, where M is the total number of repetitions.

We now show the correctness of the protocol. Our protocol is built upon two insights: (i) For a stabilizer input state, the fidelity is estimated by estimating the expectation value of the stabilizer regarding the output state, and (ii) The correction unitary U_Σ (i.e. a Pauli) can either be commute or anti-commute with the stabilizer P_{in} . In light of the two insights, we observe that the output density matrix satisfies

$$\text{tr}\{\rho_{\text{out}} P_{\text{in}}\} = \text{tr}\{U_\Sigma^\dagger \rho_{\text{in}} U_\Sigma P_{\text{in}}\} = (-1)^a \text{tr}\{\rho_{\text{in}} P_{\text{in}}\}, \quad (\text{E8})$$

by noting that $\rho_{\text{in}} = U_\Sigma \rho_{\text{out}} U_\Sigma^\dagger$. That is we can pull the correction unitary through the stabilizer up to a phase depending on the commutation relationship between the two operators. An effective way of measuring the fidelity of the teleported state thus yields without invoking feedforward quantum operations: We estimate the expectation value of the stabilizer P_{in}

and multiply the phase $(-1)^a$, which gives us the estimation of $\text{tr}\{\rho_{\text{in}}P_{\text{in}}\}$. Finally, we note that for $n \in \mathbb{Z}_{\text{even}}$ or \mathbb{Z}_{odd} , we measure the last qubit in the different basis, which we will explain in Sec. E 5.

As the quantum device is prone to readout errors, we now discuss the combination of measurement error mitigation with our post-selection-free quantum teleportation protocol. The readout errors could cause a severe deviation from the estimated fidelity of the teleported state compared to what it first appears. The rationale is rooted in the fact that the correction unitary depends on the measurement outcome of the first n qubits. As such, the incorrect measurement results resulting from the readout error are counted by an amount of $n * p_{\text{avg}}$, where p_{avg} is the average single-qubit error rate if the correlated error rate is small. Consequently, because the correction unitary depends on the measurement outcome's parity, the output state's fidelity may deteriorate linearly as the qubit number grows. This observation is verified in our experimental results in the main text Fig. 4B.

We provide details on measurement error mitigation for the TOD tasks here. In the ideal case, the fidelity between the input state ρ_{in} and the output state ρ_{out} can be expressed as:

$$\mathcal{F}(\rho_{\text{in}}, \rho_{\text{out}}) = \sum_x p(x) \text{Tr} [U(x)\rho_{\text{out}}U(x)^\dagger\rho_{\text{in}}] \quad (\text{E9})$$

where $p(x)$ is the probability distribution over the measurement outcomes. As mentioned earlier, noise can flip the measurement outcomes according to some probability distribution. Let us denote this noise by $p(y|x)$, where $x = x_1x_2 \dots x_n$ represents the input measurement results and $y = y_1y_2 \dots y_n$ represents the noisy output. For a qubit-independent readout noise model, the noise is assumed to act independently on each qubit. Hence, we can write the probability distribution of the noisy output as $p(y) = p(y_1|x_1) \dots p(y_n|x_n) \cdot p(x)$, which leads to a noisy fidelity expression

$$\tilde{\mathcal{F}} = \sum_x p(x) \sum_y p(y_1|x_1) \dots p(y_n|x_n) \text{Tr} [\rho_{\text{out}} \cdot U(y)^\dagger\rho_{\text{in}}U(y)]. \quad (\text{E10})$$

This can be approximated by performing measurements and averaging over the M measurement outcomes y_m as follows

$$\tilde{\mathcal{F}} \approx \frac{1}{M} \sum_{m=1}^M \text{Tr} [\rho_{\text{out}} \cdot U(y_m)^\dagger\rho_{\text{in}}U(y_m)], \quad (\text{E11})$$

where y_m is the m -th measurement outcome.

To mitigate the noise effect, we apply the inverse of the noise model. Specifically, the corrected fidelity can be written as:

$$\mathcal{F} = \sum_x p(x) \sum_y p(y_1|x_1) \cdots p(y_n|x_n) \sum_{x'} p^{-1}(y_1|x'_1) \cdots p^{-1}(y_n|x'_n) \times \text{Tr} [\rho_{\text{out}} \cdot U(x')^\dagger \rho_{\text{in}} U(x')], \quad (\text{E12})$$

where $p^{-1}(y|x)$ represents the inverse of the noise model. In practice, we estimate the fidelity from the measurement outcomes by averaging over M independent trials

$$\hat{\mathcal{F}} = \frac{1}{M} \sum_{m=1}^M \sum_{x'} p^{-1}(y_{m1}|x'_1) \cdots p^{-1}(y_{mn}|x'_n) \text{Tr} [\rho_{\text{out}} \cdot U(x')^\dagger \rho_{\text{in}} U(x')], \quad (\text{E13})$$

where $y_m = y_{m1}y_{m2} \cdots y_{mn}$ denotes the m -th measurement outcome, and $p^{-1}(y_i|x'_i)$ is the inverse noise function for the i -th qubit. In this expression, the term inside the trace operator lies within the range $[-1, 1]$, and the inverse noise model amplifies it. The amplification factor is characterized by the coefficient

$$\Gamma = \max_{x,y} [p^{-1}(y_1|x_1) \cdots p^{-1}(y_n|x_n)] = \prod_{i=1}^n \frac{1 + |\epsilon_i - \eta_i|}{1 - \epsilon_i - \eta_i}, \quad (\text{E14})$$

which corresponds to the tensor product overhead Γ_{TP} discussed in Eq. (D16). Thus, by similar reasoning, we can estimate the fidelity within an error bound $\epsilon = \Gamma \sqrt{\frac{2 \log(2/\delta)}{M}}$, where M is the number of measurements and the failure probability is lower than δ .

4. Fidelity oscillations in the experimental simulation of symmetry-protected topological phases

Using the circuit in the main text Fig. 4, we performed experimental simulations of the symmetry-protected phase and demonstrated its robustness against symmetry verification operations by measuring the teleportation fidelity. Specifically, we introduced a single symmetry verification operation into the circuit and scanned the variations of the phase parameter α in the operation to evaluate its impact on the teleportation fidelity. As shown in Fig. S20a, we conducted simulations on a one-dimensional 5-qubit cluster state and fitted the experimental data points using the trigonometric function $f(x) = A \sin(t/T + \theta) + B$. The fidelity fluctuation was defined as twice the amplitude of the fitted function. Results revealed that, under a single symmetry-preserving operation, the teleportation fidelity exhibited strong robustness to variations in the phase parameter, with fidelity fluctuations

below 10%. In contrast, under a symmetry-breaking operation, the robustness of fidelity to phase parameter variations depended on the input state. For input states $|\psi_{\text{in}}\rangle = |\pm\rangle$, the symmetry-protected phase retained symmetry and fidelity fluctuations remained below 10%, whereas for $|\psi_{\text{in}}\rangle = \pm|0\rangle, \pm|i\rangle$, the symmetry was broken, resulting in fidelity fluctuations exceeding 50%.

Using the same protocol, we increased the experimental scale and verified the robustness of symmetry-protected phases in teleportation circuits ranging from 5-qubit to 95-qubit scales. As shown in Fig S20, the experimental results consistently demonstrated robustness, although visibility decreased due to accumulated decoherence and gate errors as the circuit size increased.

To further validate the robustness of the symmetry-protected phase, we introduced the symmetry verification group with multi parallel symmetry verification operations and scanned the variations of the phase parameter α for 25-qubit teleportation circuits, following the same approach as the single-operation case, as shown in Fig S21. Similar to the case with a single verification operation, the results further indicated that the fidelity of teleportation exhibits the same state dependence under symmetry-breaking operations.

By comparing the results of symmetry-preserving and symmetry-breaking operations, we confirmed the impact of these operations on the robustness of the symmetry-protected phase. All experimental data were obtained without error mitigation. Additionally, we compared the fidelity data with and without error mitigation (Fig S22). The error-mitigated results showed improved fidelity performance, although the error bars remained noticeable. This indicates that further experimental repetitions are needed to reduce statistical uncertainties.

We highlight some of the exotic behavior of the experimental results and provide explanations here. First, for the case of a single symmetry-breaking unitary introduced, we observe that for $|+\rangle$ and $|-\rangle$ input states, the fidelities are stable and close to the symmetry-preserving cases as shown in Fig. S20. This manifests that for specific input states, the quantum teleportation succeeds regardless of whether the resource state is compromised or not. To explain this, we use knowledge from measurement-based quantum computation (MBQC) that is formally introduced in Sec. E5. These mathematical tools provide a general framework for identifying what properties we need from the resource state for MBQC to function. This will, in turn, help us explain why, in certain cases, even though the $\mathbb{Z}_2 \times \mathbb{Z}_2$ breaks, the quantum teleportation still succeeds; equivalently, the state still could serve as

a resource state for the specific occasion.

The quantum teleportation corresponds to the identity gate in MBQC. Taking the input state $|+\rangle$ and the number of qubits $n \in \mathbb{Z}_{\text{even}}$ in the resource cluster state as an instance. The general scheme for using MBQC to realize the universal gate set is provided by [Ref. [42], Theorem 1]. Specifically, we will apply this theorem and the deduction shown in Sec. I G (1) of Ref. [42]. In such cases, the overall state (denoted as $|\phi\rangle$) becomes a $(n + 1)$ -qubit cluster state after Step 1 of the scheme introduced in Sec. E 3. Let us note that the $e^{i\beta Z_1 X_2 Z_3}$ in the symmetry-breaking unitary will only add a global phase to the overall state as it is exponential of one of the stabilizers of the cluster state. This leaves the $e^{i\alpha Y_3}$ the term responsible for breaking the $\mathbb{Z}_2 \times \mathbb{Z}_2$ symmetry. Following Sec. I G (1) of Ref. [42], we get the resulting eigenvalue equation of the overall cluster state as

$$\prod_{i=0, i \in \mathbb{Z}_{\text{even}}}^n X_i |\phi\rangle = |\phi\rangle. \quad (\text{E15})$$

Now, adding the $e^{i\alpha Y_3}$ term gives

$$\prod_{i=0, i \in \mathbb{Z}_{\text{even}}}^n X_i |\phi'\rangle = |\phi'\rangle, \quad (\text{E16})$$

where $|\phi'\rangle = e^{i\alpha Y_3} |\phi\rangle$. Clearly, the state $|\phi'\rangle$ has the exact same $\prod_{i=0, i \in \mathbb{Z}_{\text{even}}}^n X_i$ correlation as a typical cluster state, and the rest of the deduction is similar to that of Ref. [42]. This explains the results. For other input states, such as $|0\rangle$ or $|1\rangle$, the eigenvalue equation becomes

$$Z_0 \prod_{i=1, i \in \mathbb{Z}_{\text{odd}}}^{n-1} X_i Z_n |\phi\rangle = |\phi\rangle, \quad (\text{E17})$$

which will be affected by the symmetry-breaking unitary. Yet, when the term in symmetry-breaking unitary becomes $e^{i\alpha Y_2}$, the input state $|0\rangle$ or $|1\rangle$ is unaffected. In contrast, the $|i\rangle$ and $|-i\rangle$ states depend on both preservation of the even and odd parities so that they could be more sensitive to noise.

5. Cluster states as resources for measurement-based quantum computation

The measurement-based quantum computation (MBQC) provides an alternative way to implement the quantum circuit on an input quantum state through only single-qubit measurements at the cost that encoding the logical qubits into a larger physical qubit system.

For a review of MBQC, see Ref. [25]. In this section, we review some basic notions and principles of MBQC and shed light on our experimental preparation of the cluster state, as one of the SPT phases provides the potential for realizing large-scale MBQC.

The MBQC implements the quantum circuits by single-qubit measurements. It is well known that two-dimensional cluster states can serve as resources for universal quantum computing for MBQC such that arbitrary $SU(2)$ gates and two-qubit primitive gates, such as the CNOT gate, are realizable. While for the one-dimensional case, we can only implement single-qubit gates through measurement. For a 2D cluster state supported on a constant-degree graph, i.e. graph state, we will refer to the graph as a 2D pattern. The graph is partitioned into several parts: (i) the input part, (ii) the body part, and (iii) the output part. The input part prepares the qubit in the state $|\psi_{\text{in}}\rangle$. Then, by single-qubit measurements on a pre-determined basis, the state is propagated through the body part. The resulting state is obtained in the output part such that $|\psi_{\text{out}}\rangle = U|\psi_{\text{in}}\rangle$, where U is the targeted unitary. The above process describes the basic format of MBQC. That is, there exists an underlying information flow in the measurement process such that the input becomes the output state. To explain this, we introduce the following results about MBQC.

Fact 1. *An arbitrary $SU(2)$ gate can be implemented by a 4-qubit 1D cluster state chain with feedforward quantum operations.*

Proof. An illustration of the realization can be found in [Ref. [43], Figure 21.3b], where the input qubit is on the leftmost of the 1D chain. After measuring the first 3 qubits and performing feedforward quantum operations, we obtain the aimed output state on the rightmost qubit. To realize an arbitrary $SU(2)$ gate, it suffices to decompose the gate into products of three gates through Euler angles. This is given by $U_Z(\alpha)U_X(\beta)U_X(\gamma)$, where $U_\sigma(\theta)$ is the single rotation around the σ axis of angle θ . For the derivation, we refer the readers to Ref. [42, 43]. It should be noted that the feedforward operations are determined by the measurement outcome, which is similar to the correction unitary of quantum teleportation (i.e. identity gate, as shown in Fig. S23a). \square

Fact 2. *The CNOT gate can be implemented by a 2D pattern illustrated in Fig. S23b.*

Proof. The 2D measurement pattern for the CNOT gate was first proposed by Ref. [2]. The entanglement of qubits is initially set up using control-Z (CZ) gates to form a cluster state, with subsequent measurements in specific bases generating the desired logical operations.

Consider a single qubit input state $|\psi_{\text{in}}\rangle = \alpha|0\rangle + \beta|1\rangle$ entangled with a $|+\rangle$ state via a CZ gate. After measuring the first qubit in the X -basis, the output state is:

$$|\psi_{\text{out}}\rangle = X^a H |\psi_{\text{in}}\rangle, \quad (\text{E18})$$

where $a \in \{0, 1\}$ is the measurement outcome, and the transformation is equivalent to applying a Hadamard gate, up to a Pauli X^a correction. The same effect is discussed in Ref. [43, 44].

For the CNOT gate, we consider a 2D cluster state with a control qubit C , a target qubit T , and intermediary qubits initialized in $|+\rangle$ states as shown in Fig. S23b. The control and target qubits are entangled using CZ gates. Measurement of Q2 and Q3 in the X basis results in a CNOT gate between Q1 and Q4, with Q1 being the control qubit. The reason for this implementation is simple. The measurements of Q2 and Q3 lead to two Hadamard gates (up to Pauli corrections) sandwiching the CZ gate natively prepared by the cluster state. As such, it becomes a CNOT gate. \square

It should be noted that the feedforward quantum operation is Pauli. This is not an exception; all Clifford gates executed by the MBQC have the feedforward quantum operations as Pauli operators. Besides, from the derivation of Fact 2, we also know that a single-qubit (Pauli X basis) measurement of 1D cluster state chain is equivalent to applying a Hadamard gate to the input state up to some correction unitary. We thus clarify the choice of measurement basis in Step 2 in the postselection-free fidelity estimation protocol in Sec. E3. The rationale is that for a 1D chain of $n \in \mathbb{Z}_{\text{odd}}$, the $(n - 1)$ measurement results in an even number of Hadamard gates acting on the input state so that up to some Pauli correction, we can detect the teleported state directly. Yet, for $n \in \mathbb{Z}_{\text{even}}$, the teleported state is $H|\psi_{\text{in}}\rangle$ so that the measurement basis is transformed by a Hadamard gate to account for the effect.

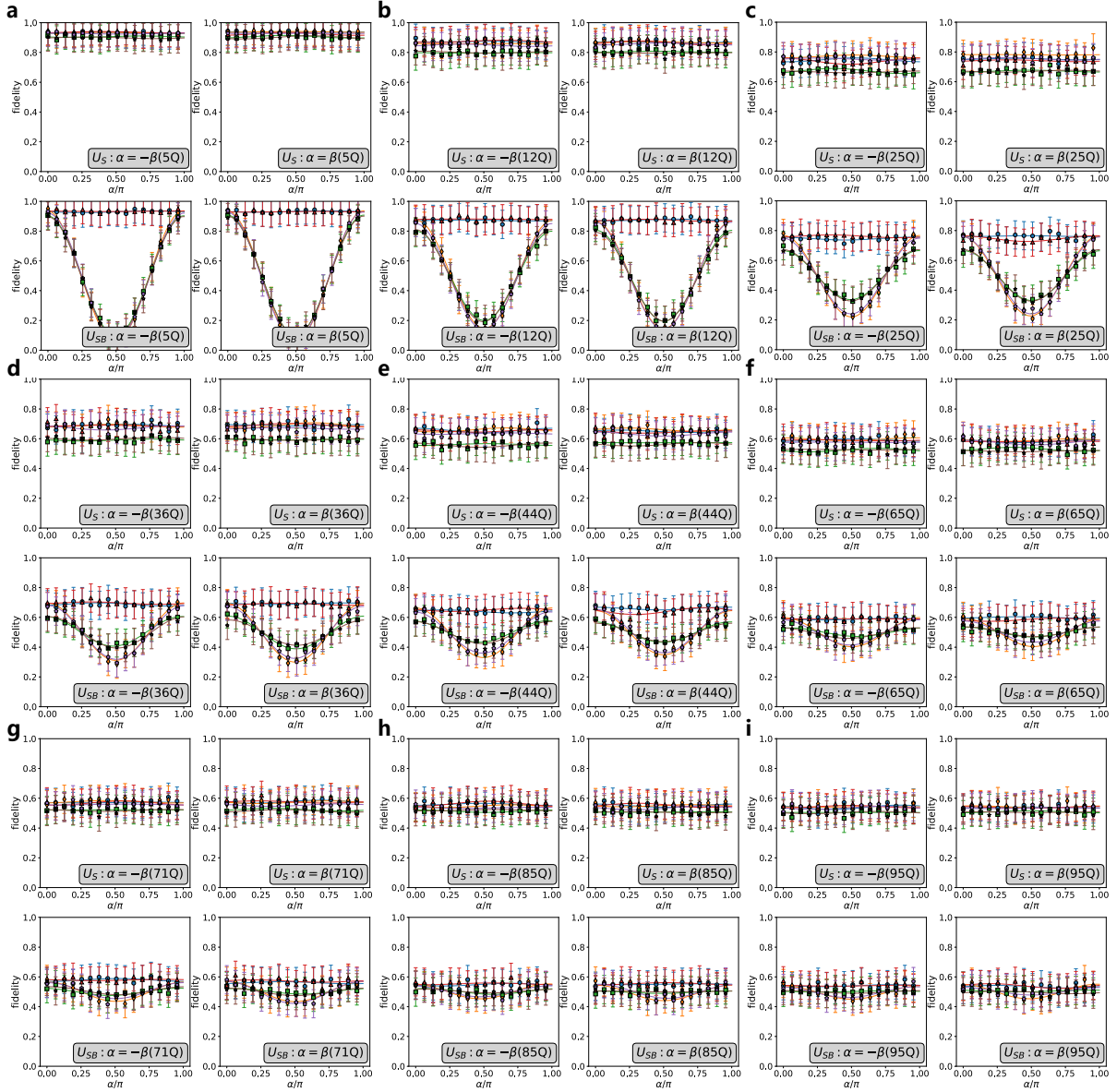


FIG. S20. Experimental teleportation fidelity versus the phase parameter α/π for different input states with 1 group of symmetry-preserving or odd-parity symmetry-breaking operation. The curves in the figure are derived from trigonometric fits to the data points, with the twice the amplitude of the fit defined as the fidelity oscillation. (a-i) contains different qubit numbers from 5Q to 95Q.

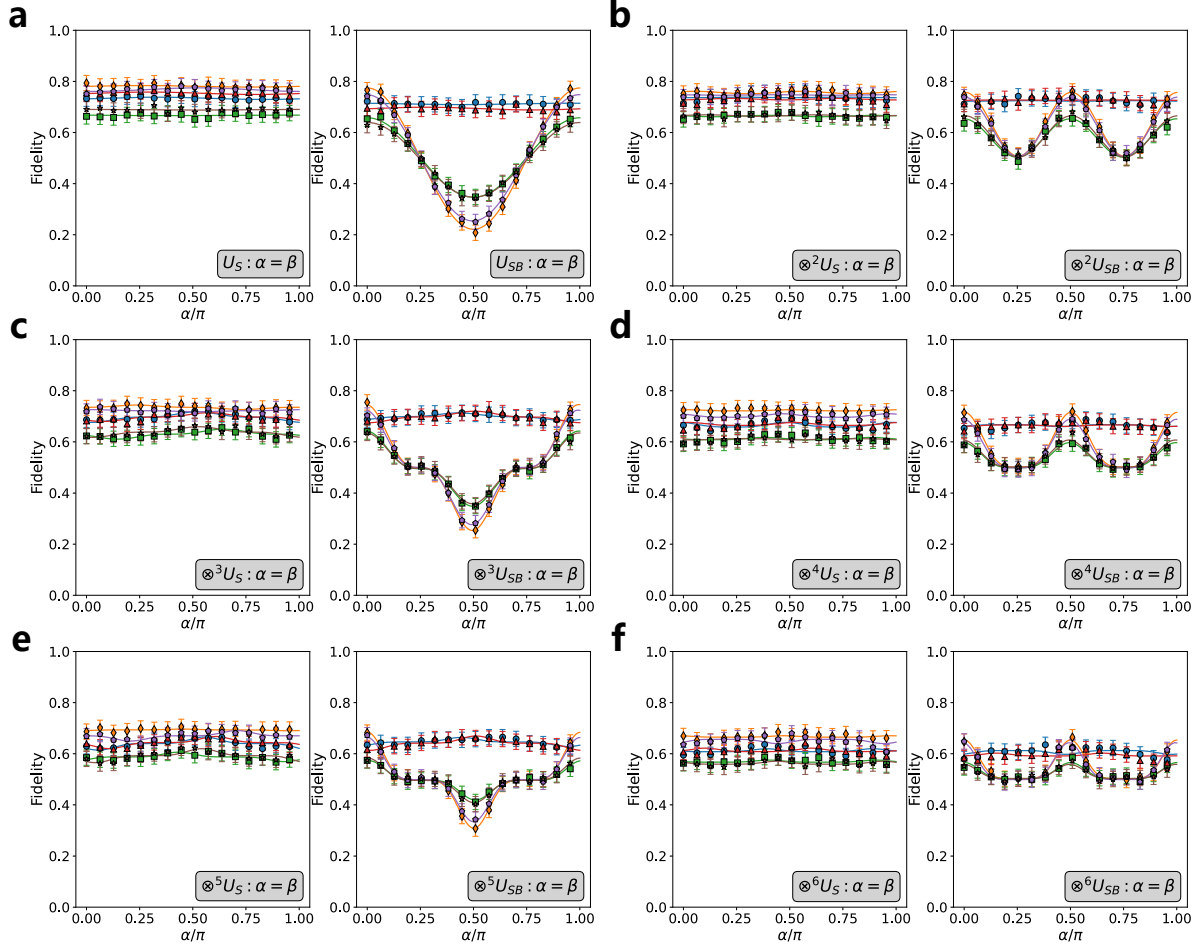


FIG. S21. Experimental teleportation fidelity as a function of the phase parameter α/π for different input states under odd-parity symmetry-breaking operations applied across multiple groups of qubits. The simulations were conducted on a teleportation circuit with 25 qubits. The curves represent fits based on trigonometric functions, with the degree of the fit matching the number of parallel groups. For instance, the data for n groups is fitted using an n -degree trigonometric function. The fidelity oscillation, defined as twice the amplitude of the fit, quantifies the oscillatory behavior. (a–f) correspond to results for one to six groups of symmetry operations applied to different qubits, respectively.

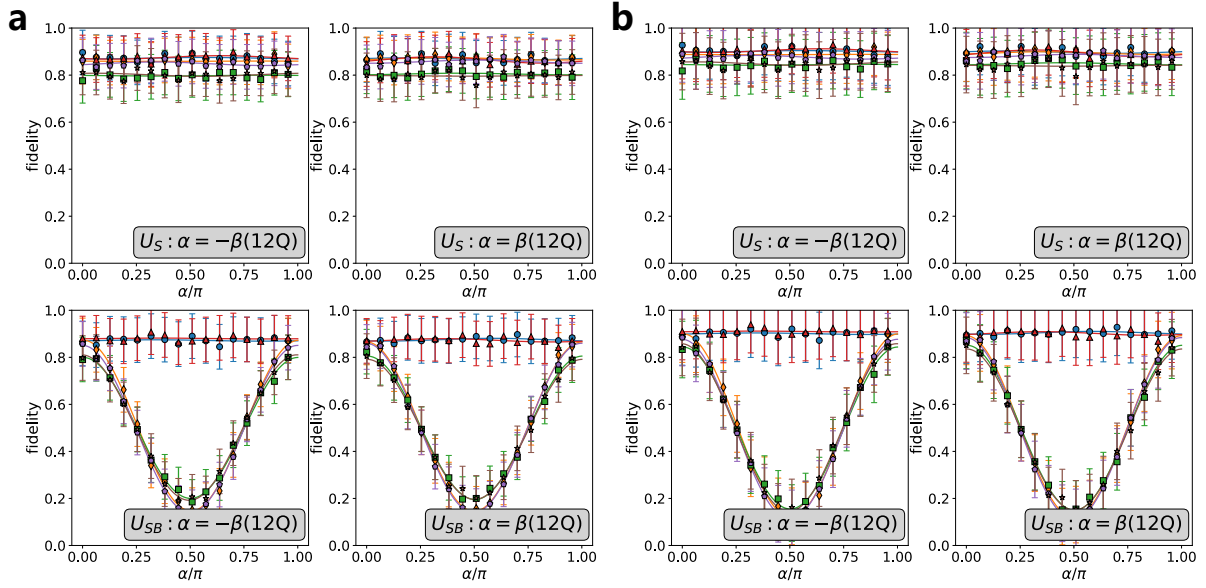


FIG. S22. Comparison between SPT results with and without readout error mitigation. The results of 12 qubits are presented here for demonstration. The curves in the figure are derived from trigonometric fits to the data points, with the amplitude of the fit defined as the fidelity fluctuation. (a) Without mitigation. (b) With mitigation.

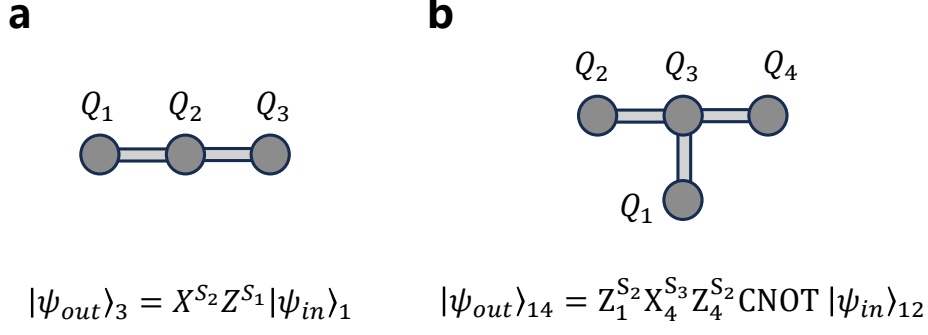


FIG. S23. Schematic illustration of MBQC implementation for the identity (I) gate and the controlled-NOT (CNOT) gate. (a) Implementation of the single-qubit I gate using a three-qubit entanglement structure following a cluster-state generation procedure. The input state $|\psi_{in}\rangle$ is initialized on qubit 1, while qubits 2 and 3 are prepared in the $|+\rangle$ state. CZ gates establish a one-dimensional chain, after which X-basis measurements on qubits 1 and 2 yield outcomes s_1 and s_2 , determining the final state of qubit 3 as $|\psi_{out}\rangle_3 = X^{s_2} Z^{s_1} |\psi_{in}\rangle_1$. The byproduct operators $X^{s_2} Z^{s_1}$ can be corrected via classical post-processing. (b) Implementation of the two-qubit CNOT gate using a four-qubit entanglement structure based on a cluster-state preparation protocol. The input state $|\psi_{in}\rangle$ is initialized on qubits 1 and 2, while qubits 3 and 4 are in $|+\rangle$. Three CZ gates are applied according to the illustrated connectivity. X-basis measurements on qubits 2 and 3 yield outcomes s_2 and s_3 , resulting in the final state $|\psi_{out}\rangle_{14} = Z_1^{s_2} X_4^{s_3} Z_4^{s_2} \cdot \text{CNOT} |\psi_{in}\rangle_{12}$, with byproduct operators corrected through post-processing.